NASA TECHNICAL MEMORANDUM

NASA TM X-52188

NASA TM X-52188

ANALYTICAL STUDY OF SOME THERMAL STRESSES IN A NUCLEAR ROCKET FUEL ELEMENT (U)

by Edward R. Hersman, Eugene J. Pleban, John S. Clark,
and Dennis P. Townsend
Lewis Research Center
Cleveland, Ohio

NATIONAL AERONAUTICS AND SPACE ADMINISTRATION · WASHINGTON, D.C. · 1966

C66-3033

CONFIDENTIAL

NASA TM X-52188

ANALYTICAL STUDY OF SOME THERMAL STRESSES IN A NUCLEAR ROCKET FUEL ELEMENT (U)

by Edward R. Hersman, Eugene J. Pleban, John S. Clark, and Dennis P. Townsend

Lewis Research Center
Cleveland, Ohio

RESTRICTED DATA
ATOMIC ENERGY ACT OF 1954

GROUP 1
Excluded from automatic downgrading and declassification

NOTICE — THIS DOCUMENT CONTAINS INFORMATION AFFECTING THE NATIONAL DEFENSE OF THE UNITED STATES WITHIN THE MEANING OF THE ESPIONAGE LAWS, TITLE 18, U.S.C., SECTIONS 793 AND 794. ITS TRANSMISSION OR THE REVELATION OF ITS CONTENTS IN ANY MANNER TO AN UNAUTHORIZED PERSON IS PROHIBITED BY LAW.

NATIONAL AERONAUTICS AND SPACE ADMINISTRATION

CONFIDENTIAL

ANALYTICAL STUDY OF SOME THERMAL STRESSES IN A NUCLEAR ROCKET FUEL ELEMENT (U)

by Edward R. Hersman, Eugene J. Pleban, John S. Clark, and Dennis P. Townsend

Lewis Research Center

SUMMARY

Reactor core reliability, essential to the successful development of nuclear rockets, can only be evaluated if core thermal stresses are known. These stresses in turn depend upon the axial and radial material temperature profiles of the fuel elements which make up the core. In order to save both time and money in obtaining the required fuel element thermal information, an electrical simulation of nuclear heating was proposed and, in addition, material temperatures were calculated for both cases.

At core operating temperatures, the fuel element lining probably flows plastically. Lack of stress-strain and brittle-ductile transition material properties for fuel element materials prevents the accurate determination of thermal stresses for elements subjected to plastic flow. As a consequence, the thermal stress calculations currently possible must be restricted to the elastic region, and since it is known that these may not be the actual fuel element stresses, only an approximate stress study can be performed.

Details of an elastic thermal stress calculation procedure are reported herein, and the method is applied to a sample fuel element to illustrate how it may be used to examine stresses in fuel elements. In addition, some considerations that are required in evaluating the validity of the results (and simulation) are included.

For the electrically heated fuel elements used as examples herein, it was found that the values of electrical resistivity of graphite had a considerable effect upon the power distribution and the wall and fluid temperatures. In addition, it was found that the niobium carbide lining temperatures for the electrically heated fuel elements were lower than those for the nuclear heated elements.

INTRODUCTION

Nuclear rocket engines currently under development (such as NERVA) employ nuclear reactors whose cores are composed for hundreds of graphite fuel elements, each of which contains numerous circular flow passages through which the hydrogen propellant passes. The ability to develop reliable fuel elements is essential to insure the success of these nuclear rocket engines. Fuel element reliability in turn requires that permissible strain levels be maintained

in the element and that corrosion of the element be minimized. To determine that both of these criteria are satisfied, it is necessary to know how to calculate the fuel element material temperatures and temperature gradients.

Analytical procedures for determining fuel element temperatures and temperature gradients, whether the element is heated electrically or by nuclear radiation, have been presented in reference 1. The analytical procedures were applied to a typical fuel element in reference 1 and showed that over most of the fuel element length, the temperatures for the element in the nuclear environment exceeded those for the electrically heated one. See "SAMPLE CALCULATIONS" for more details.

With methods available for fuel element thermal analysis, the next step is the evaluation of stress for the nuclear and electrical temperature environments. Lack of stress-strain and brittle-ductile transition property value data for fuel element materials at low and at elevated (operating) temperatures limits present day stress analyses to the elastic region. Such stresses do not necessarily represent actual fuel element stresses, and hence can only be used in an approximate way.

The report presents details of an elastic thermal stress analysis which, as mentioned previously, is applicable only in an approximate way. This theory is then applied to identical fuel elements, one heated electrically and the other by nuclear radiation, and the thermal stresses are determined.

The stress analysis considers longitudinal and radial steady-state temperature variations, the interaction between the fuel element material (graphite) and the protective passage lining (niobium carbide), and material property variations with temperature. Methods discussed in references 2, 3, and 4 are applied. For the application of the analysis, an NRX-A fuel element was selected; a nuclear case and two electrical cases (with different values of electrical resistivity of graphite) are studied.

ANALYSIS

Thermal

A detailed description of the analytical methods used for predicting fuel-element temperatures and temperature gradients for both nuclear and electrical resistance heated fuel elements is given in reference 1. Briefly, the methods consist of two computer programs: CAFF (Core Analysis-Fluid Flow) and CAM (Core Analysis-Material). The program CAFF is used to calculate fluid conditions, heat-transfer coefficients, heat fluxes, and wall temperatures as functions of axial position in a multipassage (multiorifice) core with nonuniform heat generation. The program CAM uses output data from CAFF, core

geometry data, and power generation rates as input to calculate steady-state axial and radial temperature distributions and maximum temperature gradients at each section of a three-dimensional solid with internal heat generation and convectively cooled boundaries.

Stress

An approximate fuel element elastic stress analysis is presented herein. The resulting computer program is referred to as TSAFE (Thermal Stress Analysis-Fuel Element). The symbols used are defined in Appendix A, and details of the analysis are given in Appendices B and C. A discussion of its limitations, theory and procedures is given in the following paragraphs.

The analysis presented is approximate since it is limited to the elastic range. Furthermore, the fuel element is approximated by a cylinder of niobium carbide (lining) and a cylinder of graphite (fuel) drawn concentrically about the axial coolant holes. The interactions of the adjacent graphite cylinders are ignored; the outer boundary is assumed to be stress free. The error introduced by these assumptions is not known.

At the present time there is no known, valid exact solution to the hexagonal lined fuel element problem. Therefore in order to compare the effect of nuclear heating with electrical heating on a fuel element which includes a lining, it was necessary to develop an approximation scheme.

The following considerations were included in the approximate analysis:

1. The nonlinear temperature variations in both the radial and longitudinal directions

2. The combined stiffness of the lining and the base material of the element

3. The differences in the mean coefficient of thermal expansion between the two materials

4. A thick-shell cylinder analysis

A finite cylinder method was used in the analysis. The long cylindrical model assumed is divided into a finite number of short cylinders. The length of these cylinders is chosen to satisfy the following three conditions:

1. The longitudinal temperature gradient along the length of the finite cylinder can be considered linear.

2. The finite cylinder motions must be accurately defined by rigid body motions when elastic foundation theory is used (ref. 2).

3. The effects of the radial gradient at the finite cylinder ends overlay insofar as curvature of the cylinder is concerned.

Satisfaction of these three conditions implies that each finite cylinder would deform (due to longitudinal temperature and coefficient of thermal expansion variations) into the form of a truncated cone, with the ends slightly curved due to a difference in radial gradient between the ends.

The expansion profile of the overall long cylinder then is approximated by a series of curved chords; these chord shapes being generated by the rigid body and curvature from the radial and longitudinal temperature gradient variations. At each junction of any two finite cylinders, there is a change in slope and a difference in expansion. To satisfy the uniqueness theorem, compatibility has to be restored at these junctions. Therefore, a radial moment and a shear force must be applied at each junction to restore compatibility. A set of compatibility equations have been written equating the deflection and rotation of adjacent finite cylinders. The simultaneous solution of all the compatibility equations yields finite values of the moments and shears applied. When added algebraically to the forces due to the interaction between the liner base material and the force applied by assuming a generalized plain strain condition the resultants will yield the complete load history along the cylindrical model. Once these values are obtained, the stresses and motions in the cylindrical model are obtained.

The first step in the analysis is to determine the free-body radial motion of each finite cylinder. This radial motion is affected by the longitudinal temperature gradient, radial temperature gradient and interaction between the lining (niobium carbide) and base material (graphite) including the biaxial effect between the two materials. The general expression for the radial motion at any point due to temperature effects is developed in Appendix B, (eq.(B8)). To this expression, the radial motion due to the interaction between the lining and graphite is added. The latter was derived using ordinary shrink fit methods to determine a contact pressure; knowing the contact pressure the radial motions of the liner and graphite can be found using equations set forth in reference 3. Subsequently, an overall general expression for free body radial motion was developed that includes both a radial temperature distribution and the interaction between the lining and the graphite due to differences in thermal expansion properties.

Using the radial temperature distribution at each end of a finite cylinder, the radial motion is determined for each finite cylinder. This radial motion consists of a displacement u and a rigid body rotation γ. In addition to these two motions, two other motions must be considered. These

result from the fact that a condition of generalized plane strain was assumed initially. In reality, the ends of the finite cylinder can change their curvature to a degree not anticipated by rigid body motions. The assumed stress on the cylinder ends does not exist and to partially account for this fact, a moment is calculated from this stress, reversed, and thus generates the desired change in curvature as well as making the longitudinal end stress nearer reality. This results in an additional displacement and rotation at each end of a finite cylinder. In the analysis, this displacement is designated as x and the rotation as φ. These two motions are determined by using elastic foundation theory. Therefore, the total free-body displacement δ at each end is a summation of u and x, and the total free-body rotation θ at each end is a summation of γ and φ.

The next phase of the analysis is to join the finite cylinders into a complete long cylinder. To do this the ends of each finite cylinder must be compatible with the ends of an adjacent cylinder with respect to displacement and rotation. In order to accomplish this, a moment and shear are applied at each junction. This results in a series of equations for each junction. By solving all the equations for the ends simultaneously, finite values are obtained for the moments and shear applied. Using these moments and shears, the final motion at r_c which is the neutral axis for a beam of 0.01 radian width taken from the cylinder, can be determined at any station along the length. Through the use of thick shell coefficients, the motion at any radial point can be found. Knowing the motion at any point, the strain at that point can be found and from the strain, the stresses can be determined.

SAMPLE CALCULATIONS

For the sample calculations, an NRX-A fuel element was chosen. This is the type of fuel element being developed by the Westinghouse Astronuclear Laboratory for the NERVA program and is the one for which the material temperatures and temperature gradients were calculated (ref. 1).

Description of Fuel Element

A sketch of a typical NRX-A fuel element is shown in figure 1. It is made from hexagonal fuel graphite (3/4 in. nominal across the flats), is 52 inches long, and contains nineteen 0.094 inch diameter flow passages 0.173 inch apart. The inside of each passage is lined by a vapor deposition process with 0.001 to 0.002 inch of niobium carbide; this lining prevents the flowing hydrogen from reacting with the graphite in the fuel element to form hydrocarbons. It was assumed that no cracks existed in the niobium carbide.

Materials Properties

For application of the analyses to a particular fuel element, property values of graphite and niobium carbide were required. Thermal property values of Graph-i-tite G were used; these are essentially the same as those for fueled graphite. Since both thermal and stress computations depend on property values, results reported herein can be improved as better property values become available. The property values used in the calculations are given either as constant values or as figure numbers in the following table:

	Niobium carbide	Graphite
Density, ρ, lb/in.^{3}	0.28	0.0615
Thermal conductivity, k, Btu/(sec)(in.)($^\circ$R)	Fig. 2	Fig. 2
Specific heat, c_p, Btu/(lb)($^\circ$R)	0.14	Fig. 3
Electrical resistivity, (ohm)(cm)	Fig. 4	Fig. 4
Young's modulus, E, lb/in.^{2}	Fig. 5	Fig. 5
Mean coefficient of linear expansion, α, in./(in.)($^\circ$R)	Fig. 6	Fig. 6
Poisson's ratio, ν, dimensionless	0.2	0.3

The densities of niobium carbide and graphite were obtained from references 5 and 6. The curve for electrical resistivity of niobium carbide was obtained from reference 7; the curve for thermal conductivity of niobium carbide was obtained from unpublished data. The curves for Young's modulus and mean coefficient of linear expansion for niobium carbide were obtained from reference 8. All other property values were obtained from Westinghouse data. The dashed curve for electrical resistivity of graphite was suggested by Westinghouse after the preparation of reference 1.

The possible transition change from brittle to ductile conditions would be highly important in an actual study of reliability of the coating. Unfortunately material data along this line are very sparse.

Cases Analyzed

Nuclear. - The maximum radial power occurs at the core centerline (except for fluctuations around the periphery which would be extremely difficult to analyze). Hence, a fuel element in the central fuel cluster was selected for the calculations since maximum temperature gradients will occur in this cluster. Every element in the core must be capable of withstanding this extreme case if failure is to be avoided.

For inlet conditions, a gas temperature of 248° R and a gas pressure of 689 pounds per square inch absolute were assumed. A flow rate of 0.05 pound per second, an orifice of 0.056 inch diameter, and a head loss coefficient of 1.44 were also assumed. These values were all obtained from Westinghouse data, and are intended to simulate actual operating conditions in a nuclear rocket.

Electrical. - The same inlet conditions and flow rate as those used in the nuclear case were assumed for the electrical cases. Since, in the electrical case, the flow is controlled externally, no orifice is required. The usual value of 0.5 for head loss coefficient applicable for a square cornered opening was used.

The power applied to the element was adjusted until the same steady-state outlet gas temperature as that obtained for the nuclear case was achieved. Thus, since the inlet and outlet conditions and the flow rate are the same for the nuclear and electrical case, the total heat added to the hydrogen should be the same. This requires about 1 megawatt of direct current electrical power.

It was assumed that electrical resistance heating occurred in the niobium carbide lining and the graphite fuel. For both sets of values of electrical resistivity of graphite material temperatures and temperature gradients were calculated.

Analytical Procedure

Thermal. - For the thermal calculations, the fuel element was divided into 52 one-inch sections and, because of assumed temperature symmetry, one-twelfth of a section was studied. Figure 7 shows the nodal geometry employed in this one-twelfth section. Flow rate and fluid property values were assumed to be identical in each flow passage. Details of the actual calculation procedures are given in reference 1; the temperature distributions were all determined so that the same exit gas temperature resulted for each case considered.

Stress analysis. - As previously mentioned, the fuel element was simulated by small adjoining cylinders circumscribed about each coolant passage hole (fig. 8). The analysis is conducted on one of the cylinders assuming neighboring cylinders offer negligible constraint. The cylindrical model was divided into 417 one-eight-inch lengths based on the length constraint discussed earlier and explained in Appendix B. The fuel element geometry, the temperature-dependent physical properties for graphite and niobium carbide, and the temperature distributions from CAM (ref. 1) are fed into TSAFE as input data. A detailed description of the analytical procedures used by

TSAFE for the nuclear and electric case is described in Appendix B. The output from TSAFE includes a listing of all input data as introduced for each station n and each element m, elements of the bandmatrix [A] of coefficients, resulting solution vector of redundant loads and moments at each station and the tangential and longitudinal stresses at each station.

RESULTS AND DISCUSSION

Thermal Analysis

Figure 9 shows a comparison between the nuclear and electrical heat generation rate in the fueled graphite portion of the fuel element as a function of axial position. The usual cosine-type distribution is seen for the nuclear case. At the core inlet, a rate of about 15 Btu/(sec)(in.^{3}) is noted. The rate increases rapidly and levels off to a maximum of about 58 Btu/(sec)(in.^{3}) about midway down the element and finally decreases to about 10 Btu/(sec)(in.^{3}) at the element end. The heat generation rate for the electric case with the original resistivity started at about 22.5 Btu/(sec)(in.^{3}) and continuously increased to a maximum of about 63 Btu/(sec)(in.^{3}) at the element end. The revised electrical resistivity data yielded a nearly linear function which started at about 29 Btu/(sec)(in.^{3}) and increased to about 48 Btu/(sec)(in.^{3}). The nuclear heat generation rate is much greater than either electrical case in the central portion of the fuel element; at the hot end, the opposite is true. The portions of the electrical data beyond the extremes denoted "End effect limit" on the figure should be ignored. This portion of the element is the chuck gripping area and conduction and power maldistribution effects affect the results in these areas.

Figure 10 compares the fluid temperatures as a function of axial position for the three cases considered. The nuclear and electric (original resistivity) data are the same as reported in reference 1. The curve for the electrical (revised resistivity) case is nearly linear and crosses the nuclear curve about 18 inches from the core inlet.

In figure 11 the average niobium carbide lining temperatures as a function of length are compared for the cases considered. Average niobium carbide temperature is of interest since local corrosion of the fuel element appears to be a function of this temperature. The temperatures for the nuclear cases are seen to be higher than any of the electrical cases except for about 10 inches on the cold end and about 6 inches at the hot end. Differences as high as 800° R are seen to exist from the element midlength to the 40 inch point.

Figure 12 compares the maximum material temperatures as a function of axial position. For about the first 19 inches of the electrically heated cases, the maximum temperature occurs at node 184 (see fig. 7); for the remaining length of the electrically heated cases, the maximum occurs at node 46; for the nuclear case, the maximum temperature occurs over the complete element length at node 184. The results are similar to figure 11; the nuclear case is hotter than the electrical cases except for about 8 inches on the cold end and 6 inches on the hot end. Differences as high as 1000° R are noted between the nuclear case and the electrical (original resistivity) case. Differences of 750° R are seen between the nuclear and electrical (revised resistivity) case.

Figure 13(a) and (b) compares material temperatures as a function of node location (see fig. 7) for all cases considered at station 48 and station 32, respectively. The temperatures of nodes 10, 31, 37, 38, 46, and 50 were used for the stress computations since node 46 was found to be the hottest for the electrical cases. At station 48 the temperatures for the three cases are seen to be about the same. The temperature gradients ($\Delta T/\Delta L$) are seen to be greater in the electrical cases than the nuclear case, however; this is expected since the heat generation rate for the electrical cases is greater than the nuclear case at this station (see fig. 9). In figure 13(b) the temperatures for the nuclear case are seen to be about 650° R greater than the electrical (revised resistivity) case and about 1000° R greater than the electrical (original resistivity) case. At this station the gradients are seen to be greater in the nuclear case, as expected.

Stress Analysis

The elastic analysis as used will yield strains which are too low for the lining and higher than reality for the graphite, provided the former (lining) enters a plastic stage at high operating temperatures.

Results obtained by applying the thermal stress analysis to the sample calculations are shown on figures 14 to 19. Figures 14, 15, and 16 present the longitudinal thermal stresses at the outer radius of the graphite, the juncture between the graphite and the niobium carbide lining, and at the average radius of the lining, respectively. Tangential thermal stresses at the same radii are shown in figures 17, 18, and 19, respectively.

A study of the stress curves (figs. 14 to 19) shows that extremely high stresses can be found along a substantial length of the elements, regardless of the method of heating.

The temperature gradients in the tangential and radial directions in the graphite portion of the fuel element in themselves cause only minor stress and could be ignored. The main stress causing effect in the fuel element is due primarily to the different mean coefficients of linear expansion of niobium carbide and graphite.

Figure 6 indicates that there is a severe abrupt change in slope of the mean coefficient of linear expansion curve for niobium carbide at around 3740° R. A study of the stress curves (figs. 14 to 19) in conjunction with a typical axial temperature profile curve (fig. 12) shows an abrupt increase in stress rate which reflects the above change in the coefficient of linear expansion

Other Considerations

The degree of prestressing induced by the coating process is at present beyond the "state-of-the-art". The carbide is deposited in a stress-free condition but is in a tensile stress condition upon cooling since its coefficient of contraction is greater than that of the graphite. The degree of prestress induced by the cooling operation after the coating process is a measure of the ability of the lining to act without fracture at the operating temperatures of the reactor. At fabrication temperatures in excess of 3000° F, the lining is much more likely to fracture in tension during cooldown. If during the coating process, stringent temperature control is not maintained on the element and the temperature is somewhat in the neighborhood of 3000° F, inconsistent cracking upon cooling down could develop in the lining.

Upon heating in the operating stages of the reactor, the lining tends to enter into a compressive stage which reduces the prestress. When the operating temperature is high enough, the prestress induced by the manufacturing process is eliminated. If the temperature at operating conditions is substantially higher than the fabrication temperature, the tensile strains upon cooling down from operating may crack the lining.

The mean coefficient of linear expansion data used indicates that if the niobium carbide is heated to high temperatures, even without load, it will not return to its original length. The temperature range where this becomes effective is not known, nor is the reason for it defined. If the operating temperatures of the reactor are high enough and the niobium carbide does not return to its original length upon cooling down, the tendency to fracture will be reduced when the fuel element reaches normal room temperature. Substantial material testing of niobium carbide must be made if guess work is to be eliminated from the coating failure picture.

CONCLUDING REMARKS

The revised electrical resistivity data (as a function of temperature), which was obtained from Westinghouse data, yields a more nearly uniform heat generation profile within the electrically heated fuel elements. As a result, the large differences in temperatures between the nuclear and electrical (original resistivity) cases has been reduced somewhat. However, the temperatures of a nuclear heated element are still greater than the temperatures in the electrical simulation except for a few inches on each end of the element. The electrically heated fuel elements had a lower niobium carbide lining temperatures than nuclear heated elements over most of the element length.

The main stress causing effect in the fuel element is the difference between the mean coefficients of linear expansion of niobium carbide lining and graphite. An anomaly exists in the reported coefficient of linear expansion for niobium carbide which produced a significant stress rate change when the material temperature exceeds 3740° R.

Lewis Research Center,
National Aeronautics and Space Administration,
Cleveland, Ohio, March 10, 1966.

APPENDIX A

SYMBOLS

A	area, $in.^2$
$B_1 - B_6$	elastic foundation coefficients (see eqs. (C38), (C39), (C45), (C46), (C47), and (C48))
C_1, C_2	constants of integration
C_3	uniform axial stress, σ_z, psi
c_p	specific heat of material, $(Btu)(lb^{-1})(^oR^{-1})$
D	flexural rigidity, $lb\ in.^2$
E	modulus of elasticity, psi
H_1, H_2, H_3	thick cylinder correction coefficients (see eqs. (C29), (C32), and (C34))
h	distance to an equilibrium position, in.
I	moment of inertia, $in.^4$
K	foundation spring constant, $in.^{-1}$
k	thermal conductivity, $(Btu)(sec^{-1})(in.^{-1})(^oR^{-1})$
l	length, in.
M	moment which helps to hold the element in a condition of plain strain, in. lb
Me	concentrated moment, in. lb
Ml	pure moment of unit value, in. lb
m	element of cylinder
P	an unknown couple force, lb
p	pressure force, psi
p_a	uniform pressure present as the result of a circumferential cut, psi

p_c pressure force to restore compatibility, psi

p_s shrink-fit pressure force, psi

Q a couple force replacing an applied unit moment, lb

RM redundant moment at station n, in. lb

RP redundant force at station n, lb

R_o electrical resistivity

r radius, in.

rx distance from origin to neutral axis, in.

S defined by equation (C20)

T an expression for the temperature distribution at any radius r, ^oR

t temperature, ^oR

u radial displacement at any radius r, in.

V concentrated shear force, lb

x radial deflection due to M, in.

y distance from a centroidal axis to an elemental area r dr dβ

α coefficient of thermal expansion, $^oR^{-1}$

β half angle of sector, radians

γ rigid body end rotation, radians

Δ total radial deflection including effects of redundants, in. (see eq. (B37))

δ total free radial deflection, in. (see eqs. (B34) or (B35))

ϵ elongation, in. in.$^{-1}$

Θ total end rotation including effects of redundants, radians (see eq. (B38))

θ total free end rotation, radians

λ elastic foundation parameter, in.$^{-1}$

ν Poisson's ratio

σ stress, psi

Φ end rotation due to Me, radians

φ end rotation due to M, radians

[A] matrix of coefficients of the unknowns, $n \times n$

[D] column matrix of constant elements, $n \times 1$

[R] column matrix of unknowns, $n \times 1$

Subscripts:

a cylinder part a

b cylinder part b

c composite section

eq equivalent

G outer cylinder or outer sector

i inside

j juncture

M mean

m element

max maximum

N inner cylinder or inner sector

n station ($1 \leq n \leq 417$)

o outside

r radial

t tangential

tot total

x restoring moment, $P(rx_G - rx_N)$

Z longitudinal (axial)

Subscript:

' part of a whole

APPENDIX B

THERMAL STRESS ANALYSIS OF A FUEL ELEMENT (TSAFE)

An approximate thermal stress analysis study was programmed to solve for the displacements and stresses of a cylindrical fuel element due to steady-state temperature conditions in the reactor. The analysis was coded in Fortran IV language to be accepted by the IBM D-C 7044/7094 computer system. The program accepts the fuel element geometry, material physical properties and temperature data as input.

ASSUMPTIONS:

The following assumptions were used as a basis for the formulation of the analysis:

1. The materials involved are of a homogeneous elastic nature.

2. The hexagon cross section of the fuel element was simulated by identical adjoining cycliders circumscribed about each flow hole as shown in figure 8(a). The radial constraints imposed by neighboring cylinders are neglected.

3. The temperature distribution, specified at radial positions of a cylinder section, are symmetric with respect to the longitudinal axis of the cylinder.

The following input data are required:

1. Total fuel element length.

2. Number of stations along the length of the fuel element.

3. Constant distance between stations; i.e., length of each finite cylinder. This length must satisfy the conditions of equation (C35).

4. The number of radial positions (layers) through the cylinder thickness. (Limited to a maximum 5 radii).

5. The radii from the cylinder axis to each radial position.

6. Average Poisson's ratio for both the lining material and the cylinder material.

7. Polynomial coefficients and degree of the least squares curve fit of the longitudinal (axial) temperature distribution data at each radial position.

8. In lieu of 7, a discrete map of temperature values at each radial layer for each station along the length.

In addition to the above data the following physical properties as a function of temperature (^{o}F) are required:

(a) Modulus of Elasticity as a function of temperature (^{o}F).

(b) Mean coefficient of Linear Expansion as a function of temperature (^{o}F).

DERIVATION OF THE EQUATIONS USED IN THE CALCULATION PROCEDURE

The hexagonal shaped fuel element was replaced by a single cylinder model containing an internal lining (see fig. 8). The model used is a direct result of assumption 2. The cylinder is divided longitudinally into finite lengths. The maximum value of a particular length is a function of the parameter λl_m from the theory of beams on elastic foundation (ref. 2). Analysis of the cylinder for thermal stresses was by the "finite cylinder method" which is similar to the analysis of beams of variable flexural rigidity found in reference 2, and consists of three distinct parts.

In the first part, end rotations and radial deflections are calculated in the free state at each station (division) of the cylinder model due to the given radial and longitudinal (axial) temperature distributions and their secondary effects.

Compatibility equations for slope and deflection between cylinder ends are derived in the second part. The third part is concerned with the solution of the above equations to yield redundant moments and shears at each cylinder station which, in turn, are used to calculate final motions and equivalent stresses at any point on the complete cylinder.

Part I - Derivation of Radial Deflection and End Rotation Equations

A. Radial deflection equations. - Given T, an expression for the temperature at any radius r, the radial motion at any radius r of a cylinder with concentric circular hole will be derived from basic equations found in reference 4. The subscript n identifying every equation in this subpart with a station n along the length will be omitted here; the subscript n will be inserted later, when necessary.

The general equation for the radial deflection u at any radius r at any station n along the length of a cylinder under full longitudinal restraint (plane strain) is:

$$u = \frac{1 + \nu}{1 - \nu} \frac{\alpha}{r} \int_{r_i}^{r} Tr \, dr + C_1 r + \frac{C_2}{r} \tag{B1}$$

where C_1 and C_2 are determined from boundary conditions.

The displacement u is affected by a uniform axial stress $\sigma_Z = C_3$ (ref. 4, p. 409). The additon of the term $-\nu C_3 r/E$ to the right side of equation (B1) represents the effect on u of this uniform stress on the cylinder end.

From reference 4, page 409, equation (239f), the general expression for axial stress under the condition of plane strain is:

$$\sigma_Z = - \frac{\alpha E T}{1 - \nu} + \frac{2\nu E C_1}{(1 + \nu)(1 - 2\nu)} \tag{B2}$$

The resultant of the axial stress for a cylinder with an inside radius r_i and outside radius r_o is:

$$2\pi \int_{r_i}^{r_o} \sigma_Z r \, dr = - \frac{2\pi\alpha E}{1 - \nu} \int_{r_i}^{r_o} Tr \, dr + \frac{2\pi\nu E C_1 (r_o^2 - r_i^2)}{(1 + \nu)(1 - 2\nu)} \tag{B3}$$

The resultant of the uniform axial stress C_3 is: $C_3\pi(r_o^2 - r_i^2)$. The value of C_3 which makes the total axial force zero, is obtained by adding the resultants and solving for C_3 as explained in reference 4, pages 399 to 401:

$$C_3 = \frac{2\alpha E}{(1 - \nu)(r_o^2 - r_i^2)} \int_{r_i}^{r_o} Tr \, dr - \frac{2\nu E C_1}{(1 + \nu)(1 - 2\nu)} \tag{B4}$$

Equation (B1) including effects of C_3 now becomes:

$$u = \frac{(1 + \nu)}{(1 - \nu)} \frac{\alpha}{r} \int_{r_i}^{r} Tr \, dr + C_1 r + \frac{C_2}{r}$$

$$- \frac{\nu r}{E} \left[\frac{2\alpha E}{(1 - \nu)(r_o^2 - r_i^2)} \int_{r_i}^{r_o} Tr \, dr - \frac{2\nu E C_1}{(1 + \nu)(1 - 2\nu)} \right] \qquad (B5)$$

From reference 4, page 412:

$$C_1 = \frac{(1 + \nu)(1 - 2\nu)\alpha}{(1 - \nu)(r_o^2 - r_i^2)} \int_{r_i}^{r_o} Tr \, dr \qquad (B6)$$

$$C_2 = \frac{(1 + \nu)\alpha r_i^2}{(1 - \nu)(r_o^2 - r_i^2)} \int_{r_i}^{r_o} Tr \, dr \qquad (B7)$$

Substituting (B6) and (B7) into (B5) the deflection u at any radius r is:

$$u' = \frac{\alpha'}{(1 - \nu) r (r_o^2 - r_i^2)} \left\{ (1 + \nu)(r_o^2 - r_i^2) \int_{r_i}^{r} Tr \, dr \right.$$

$$\left. + \left[r^2 (1 - 3\nu) + r_i^2 (1 + \nu) \right] \int_{r_i}^{r_o} Tr \, dr \right\} \qquad (B8)$$

where the prime (') superscript denotes part of the total free deflection. For a composite cylinder (fig. 20) the free deflections at a radial position of the outer cylinder (G) (r_o, r_c, and r_j) with no interactions from the inner cylinder (N) are:

$$u'_o = \frac{\alpha_G}{(1 - \nu_G)r_o(r_o^2 - r_j^2)} \left\{ \left[(1 + \nu_G)(r_o^2 - r_j^2) + r_o^2(1 - 3\nu_G) + r_j^2(1 + \nu_G) \right] \int_{r_j}^{r_o} Tr\, dr \right\} \quad (B9)$$

$$u'_c = \frac{\alpha_G}{(1 - \nu_G)r_c(r_o^2 - r_j^2)} \left\{ (1 + \nu_G)(r_o^2 - r_j^2) \int_{r_j}^{r_c} Tr\, Dr + \left[r_c^2(1 - 3\nu_G) + r_j^2(1 + \nu_G) \right] \int_{r_j}^{r_o} Tr\, dr \right\} \quad (B10)$$

$$u'_{j,G} = \frac{\alpha_G}{(1 - \nu_G)r_j(r_o^2 - r_j^2)} \left\{ r_j^2 \left[(1 - 3\nu_G) + (1 + \nu_G) \right] \int_{r_j}^{r_o} Tr\, dr \right\} \quad (B11)$$

Similarly the free deflections of the inner cylinder (N) at r_j and r_i are:

$$u'_{j,N} = \frac{\alpha_N}{(1 - \nu_N)r_j(r_j^2 - r_i^2)} \left\{ (1 + \nu_N)(r_j^2 - r_i^2) \int_{r_i}^{r_j} Tr\, dr + \left[r_j^2(1 - 3\nu_N) + r_i^2(1 + \nu_N) \right] \int_{r_i}^{r_j} Tr\, dr \right\} \quad (B12)$$

$$u'_i = \frac{\alpha_N}{(1 - \nu_N)r_i(r_j^2 - r_i^2)} \left\{ r_i^2 \left[(1 - 3\nu_N) + (1 + \nu_N) \right] \int_{r_i}^{r_j} Tr\, dr \right\} \quad (B13)$$

B. End rotation equations. - The rotation of element m at station n is due to (1) the difference between the radial displacements at each end and (2) the reversal of a moment which helps to hold the ends of the element

m in plane strain. The rigid body rotation at the neutral radius r_c of the element m due to the radial displacements at both ends of element m is given by the expression (fig. 21):

$$\gamma_{c,n} = \frac{u_{c,n} - u_{c,n+1}}{l} = \gamma_{c,n+1} \tag{B14}$$

Clockwise rotation is assumed plus (+).

The moment, corrected for a 0.01 radian section, which helps to hold the element m in a condition of plane strain at station n is obtained from the expression:

$$M_n = 0.01 \int_{r_i}^{r_o} \sigma_z y_c r \, dr = 0.01 \left(\int_{r_j}^{r_o} \sigma_{z_G} y_c r \, dr + \int_{r_i}^{r_j} \sigma_{z_N} y_c r \, dr \right) \tag{B15}$$

The longitudinal stresses σ_{z_G} and σ_{z_N} are due to the radial temperature distribution and an assumed couple force P_c (fig. 22).

C. Compatibility at the junction radius r_j. - To determine the free-bodied deformations of each element at a station, compatibility between the lining and the base material at radius r_j must be satisfied. Two unknown forces must be determined; (1) a radial contact pressure, p, due to the difference in physical properties (α_G, α_N, etc.) and, (2) a couple force P_c, which restores longitudinal compatibility (fig. 22). To obtain the values of P_c and p simultaneous solution of the free body deformation equations in the radial and the longitudinal direction for each element is required.

The free-bodied radial displacement (eqs. (B11) and (B12)) due to T, (ref. 3, p. 241) due to p and a Poisson's effect due to P_c are set equal at radial position r_j:

$$u'_{j,G} + \frac{r_j p}{E_G} \left(\frac{r_j^2 + r_o^2}{r_o^2 - r_j^2} + \nu_G \right) - \frac{P_c r_j \nu_G}{A_G E_G} = u'_{j,N} - \frac{r_j p}{E_N} \left(\frac{r_i^2 + r_j^2}{r_j^2 - r_i^2} - \nu_N \right) + \frac{P_c r_j \nu_N}{A_N E_N} \tag{B16}$$

The free-bodied axial displacement of a composite section of unit length (fig. 22) due to P_c, C_3, and p are set equal at a station:

$$\frac{P_c}{A_G E_G} + \frac{C_{3,G}}{E_G} - \frac{2\nu_G p r_j^2}{E_G(r_o^2 - r_j^2)} = -\frac{P_c}{A_N E_N} + \frac{C_{3,N}}{E_N} + \frac{2_N p r_j^2}{E_N(r_j^2 - r_i^2)} \qquad (B17)$$

where the approximate value of a uniform axial stress due to a radial temperature distribution across section G is

$$C_{3,G} = \frac{2\alpha_G E_G}{(r_o^2 - r_j^2)} \int_{r_j}^{r_o} Tr\, dr \qquad (B18)$$

and the approximate value of a uniform axial stress due to a mean value of the radial temperature distribution across cylinder N is

$$C_{3,N} = \alpha_N E_N T_M \qquad (B19)$$

Equations (B16) and (B17) are solved simultaneously for P_c and p at each station.

D. Total free body motions at r_c. - The deformation of a cylinder due to an external pressure p_o and an internal pressure p_i is given by equation (207), reference 3 as:

$$u = \left(\frac{1 - \nu}{E}\right)\left(\frac{r_i^2 p_i - r_o^2 p_o}{r_o^2 - r_i^2}\right) r + \left(\frac{1 + \nu}{E}\right)\left[\frac{r_i^2 r_o^2 (p_i - p_o)}{(r_o^2 - r_i^2) r}\right] \qquad (B20)$$

By substututing $p_o = 0$, $p_i = p$ into equation (B20) the free radial deformation of cylinder (G) at r_o due to p and the radial temperature distribution T:

$$u_o = \frac{2 r_o r_j^2 p}{E_G(r_o^2 - r_j^2)} + u_o' - \frac{P_c r_o \nu_G}{A_G E_G} \qquad (B21)$$

Similarly the total free radial deformation of cylinder (G) at r_c and r_j is:

$$u_c = \frac{r_j^2\left[r_c^2(1 - \nu_G) + r_o^2(1 + \nu_G)\right] p}{E_G(r_o^2 - r_j^2) r_c} + u_c' - \frac{P_c r_c \nu_G}{A_G E_G} \qquad (B22)$$

$$u_{j,G} = \frac{r_j\left[r_j^2(1 - \nu_G) + r_o^2(1 + \nu_G)\right]p}{E_G(r_o^2 - r_j^2)} + u'_{j,G} + \frac{P_c r_i \nu_N}{A_N E_N} \tag{B23}$$

The total free radial deformation of cylinder N at r_i is obtained similarly by setting $r = r_i$, $p_o = p$, $p_i = 0$

$$u_i = -\frac{2r_i r_j^2 p}{E_N(r_j^2 - r_i^2)} + u'_i \tag{B24}$$

Applying equation (246) from reference 4, and adding to this equation the direct stress due to P_c the expression for the axial stress σ_z for cylinder G (fig. 22):

$$\sigma_{z,G} = \frac{\alpha_G E_G}{(1 - \nu_G)}\left[\frac{2}{(r_o^2 - r_j^2)}\int_{r_j}^{r_o} Tr\, dr - T\right] + \frac{P_c}{A_G} \tag{B25}$$

Similarly for cylinder N:

$$\sigma_{z,N} = \frac{\alpha_N E_N}{(1 - \nu_N)}\left(\frac{t_j - t_i}{2}\right) - \frac{P_c}{A_N} \tag{B26}$$

The end rotation φ and the radial deflection x of cylinder element m at section n due to the reversal of M_n and M_{n+1} is evaluated at the radius r_c using elastic foundation coefficients (eqs. (C45) to (C48) and fig. 23):

$$\varphi_{c,n,m} = -M_n B_{5,m} + M_{n+1} B_{6,m} \tag{B27}$$

$$\varphi_{c,n+1,m} = M_{n+1} B_{5,m} - M_m B_{6,m} \tag{B28}$$

$$x_{c,n,m} = -M_n B_{3,m} + M_{n+1} B_{4,m} \tag{B29}$$

$$x_{c,n+1,m} = M_{n+1} B_{3,m} + M_n B_{4,m} \tag{B30}$$

The total free body motions at r_c of element m are:

$$\theta_{c,n} = \gamma_{c,n} + \varphi_{c,n} \tag{B31}$$

$$\theta_{c,n+1} = \gamma_{c,n+1} + \varphi_{c,n+1} \tag{B32}$$

$$\delta_{c,n} = u_{c,n} + x_{c,n} \tag{B33}$$

$$\delta_{c,n+1} = u_{c,n+1} + x_{c,n+1} \tag{B34}$$

Part II. Compatibility Equations

Since the cylinder is a continuous structure the following physical compatibility exists between the final deflections and rotations at station n (fig. 23):

$$\Delta_{c,n,m-1} = \Delta_{c,n,m} \tag{B36}$$

$$\Theta_{c,n,m-1} = \Theta_{c,n,m}$$

Expanding the above equations using the results of the previous part (eqs. (B31) to (B34)) and elastic foundation coefficients (eqs. (C36) to (C48)) applied to the unknown redundant shear, RP_n and moment, RM_n, at each station n:

$$\varphi_{c,n,m-1} + RM_n B_{3,m-1} - RP_n B_{1,m-1} - RM_{n-1} B_{4,m-1} + RP_{n-1} B_{2,m-1}$$

$$= \varphi_{c,n,m} + RM_n B_{3,m} + RP_n B_{1,m} - RM_{n+1} B_{4,m} - RP_{n+1} B_{2,m} \tag{B37}$$

$$\theta_{c,n,m-1} - RM_n B_{5,m-1} + RP_n B_{3,m-1} + RM_{n-1} B_{6,m-1} + RP_{n-1} B_{4,m-1}$$

$$= \theta_{c,n,m} + RM_n B_{5,m} + RP_n B_{3,m} - RM_{n+1} B_{6,m} + RP_{n+1} B_{4,m} \tag{B38}$$

Introducing the boundary conditions $RP_1 = RM_1 = RP_n = RM_n = 0$ and rearranging the above equations at each station the following matrix formulation is obtained

$$[A] \begin{bmatrix} RM_2 \\ RP_2 \\ \vdots \\ RM_{n-1} \\ RP_{n-1} \end{bmatrix} \begin{bmatrix} \delta_{c,2,2} - \delta_{c,2,1} \\ \theta_{c,2,2} - \theta_{c,2,1} \\ \vdots \\ \delta_{c,n-1,m} - \delta_{c,n-1,m} \end{bmatrix} \quad \text{or} \quad [A]\,[R] = [D] \tag{B39}$$

Where [A] is a symmetric band matrix of coefficients of the unknowns RP_n, RM_n.

Part III. Calculation of Final Displacements and Stresses

Solution of the above matrix equation yields the unknown moments and shears which substituted into any side of equations (B37) and (B38) yields the final motions at r_c of element m at station n, for example

$$\Delta_{c,n,m} = \delta_{c,n,m} + RM_n B_{3,m} + RP_n B_{1,m} - RM_{n+1} B_{4,m} - RP_{n+1} B_{2,m} \quad \text{(B39)}$$

Using the coefficient H_1, H_2, and H_3 derived in Appendix C the final motions at r_o, r_i, and r_j at station n:

$$\Delta_{o,m} = u_{o,n} + H_1(x_{c,n} + \Delta_{c,n} - \delta_{c,n}) \quad \text{(B40)}$$

$$\Delta_{i,n} = u_{i,n} + H_2(x_{c,n} + \Delta_{c,n} - \delta_{c,n}) \quad \text{(B41)}$$

$$\Delta_{j,n} = u_{j,n} + H_3(x_{c,n} + \Delta_{c,n} - \delta_{c,n}) \quad \text{(B42)}$$

The subscript m is redundant and will not be used below. The final longitudinal stresses at station n are calculated by adding the effect of the plane strain moment M_n (eq. (B15)) minus the redundant moment RM_n to the uniform axial stress (eq. (B25) or (B26)) evaluated at station n;

$$\sigma_{z,o,n} = \sigma_{z,G,n} + \frac{(M_n - RM_n)(r_o - r_c)}{I_G} \quad \text{(B43)}$$

$$\sigma_{z,j,n} = \sigma_{z,G,n} - \frac{(M_n - RM_n)(r_c - r_j)}{I_G} \quad \text{(B44)}$$

$$\sigma_{z,i,j} = \sigma_{z,N,n} - \frac{(M_n - RM_n)(r_c - r_i)}{I_G} \quad \text{(B45)}$$

I_G is defined in Appendix C, equation (C3).

From reference 4, equation (239), the general stress-strain relation for the tangential strain component ϵ_t is:

$$\epsilon_t = \alpha T + \frac{1}{E}[\sigma_t - \nu(\sigma_r + \sigma_z)] \quad \text{(B46)}$$

From the same reference, equation (178)

$$\epsilon_t = \frac{u}{r}$$

Rearranging and substituting $\alpha = \alpha_G$, $\sigma_r = \sigma_{r,o} = 0$, $\sigma_z = \sigma_{z,o}$, $E = E_G$, $T = T_{r,o}$, $\nu = \nu_G$, $\epsilon_t = \Delta_o/r_o$, the tangential stress at r_o is:

$$\sigma_{t,o} = E_G \frac{\Delta_o}{r_o} - E_G \alpha_G T_{r,o} + \nu_G \sigma_{z,o} \tag{B47}$$

where the subscript n was deleted for clarity.

Similarly at r_j:

$$\sigma_{t,j} = E_G \frac{\Delta_j}{r_j} - E_G \alpha_G T_{r,j} + \nu_G \sigma_{z,j} \tag{B48}$$

At r_i substituting $\alpha = \alpha_N$, $\sigma_r = \sigma_{r,i} = 0$, $\sigma_z = \sigma_{z,i}$, $E = E_N$, $T = T_{r,i}$, $\nu = \nu_N$, the tangential stress is:

$$\sigma_{t,i} = E_N \frac{\Delta_i}{r_i} - E_N \alpha_N T_{r,i} + \nu_N \sigma_{z,i} \tag{B49}$$

APPENDIX C

DEVELOPMENT AND SUMMARY OF SECTION PROPERTIES, PHYSICAL PARAMETERS AND COEFFICIENTS USED IN APPENDIX B

The following list of properties, parameters and coefficients, used in Appendix B are developed, defined and summarized:

1. Moment of inertia and centroidal distance of a sector.

2. Radius to the neutral axis of a composite section based on geometry and stiffness.

3. Equivalent flexural rigidity of a composite section.

4. Spring constant of a 0.01 radian sector.

5. Thin shell analysis correction factors.

6. Summary of beam on elastic foundation coefficients.

Moment of Inertia for a Sector of Cylinder G About Its Neutral Axis

From the mechanics of section properties (fig. 24)

$$I_G = \int_A y^2 dA = 2\int_0^{\beta}\int_{r_j}^{r_o} (rx_G - r\cos\beta')^2\, r\, dr\, d\beta'$$

$$I_G = rx_G^2(r_o - r_j^2)\beta - \frac{4}{3}\, rx_G(r_o^3 - r_j^3)\sin\beta + \frac{1}{4}(r_o^4 - r_j^4)(\beta + \sin\beta\cos\beta) \qquad (C1)$$

Distance from the origin O to the neutral axis of the sector is

$$rx_G = \frac{\int_0^{\beta}\int_{r_j}^{r_o} r\cos\beta'\, r\, dr\, d\beta'}{\int_0^{\beta}\int_{r_j}^{r_o} r\, dr\, d\beta'} = \frac{2}{3}\cdot\frac{(r_o^3 - r_j^3)}{(r_o^2 - r_j^2)}\cdot\frac{\sin\beta}{\beta} \qquad (C2)$$

Substituting rx_G into equation (C1), the moment of inertia of a sector about its own neutral axis is:

$$I_G = \frac{1}{4} \cdot (r_o^4 - r_j^4) \cdot (\beta + \sin\beta \cos\beta) - \frac{4}{9} \cdot \frac{(r_o^3 - r_j^3)^2}{(r_o^2 - r_j^2)} \frac{\sin^2\beta}{\beta} \qquad (C3)$$

Radius to the Neutral Axis of a Composite Section Based on Geometry and Relative Stiffness

The neutral axis rx_c (fig. 25) of a cylinder sector with a lining (composite section) based on geometry and relative stiffness is obtained by investigating the resistance to bending and elongation the section provides to an applied end moment M1 = 1 inch pound (double arrow signifies a moment, right hand rule is assumed). The expression for the couple force Q applied at rx_G and -Q applied at rx_N which replaces the moment M1 (fig. 26) is:

$$Q = \frac{M1}{rx_G - rx_N} = \frac{1}{rx_G - rx_N} \qquad (C4)$$

where rx_N is defined as average radius of the lining $N = (r_j + r_i)/2$. Assuming plane strain the G sector elongates due to Q by an amount (ref. 4, p. 24)

$$\epsilon'_{z,G} = \frac{Q\left(1 - \nu_G^2\right)}{A_G E_G} \qquad (C5)$$

simultaneously N sector compresses:

$$\epsilon'_{z,N} = - \frac{Q\left(1 - \nu_N^2\right)}{A_N E_N} \qquad (C6)$$

Ignoring the bending resistance of N, compatibility between the sectors is restored in terms of a second couple force P as shown in figure 26. Translation of the couple force P from the r_j to rx_G creates a moment $P(rx_G - rx_N)$, where rx_N is substituted for r_j to simplify derivations to follow. Strain on sector G at r_j due to the above moment is:

$$\epsilon'_{z,x} = - \frac{P(rx_G - rx_N)^2(1 - \nu_G^2)}{E_G I_G} \qquad (C7)$$

Using equations (C5) to (C7) and including the effect of P in the same manner as Q in equations (C5) and (C6) compatibility at r_j is restored by:

$$\frac{Q(1 - \nu_G^2)}{A_G E_G} - \frac{P(1 - \nu_G^2)}{A_G E_G} - \frac{P(rx_G - rx_N)^2(1 - \nu_G^2)}{E_G I_G}$$

$$= - \frac{Q(1 - \nu_N^2)}{A_N E_N} + \frac{P(1 - \nu_N^2)}{A_N E_N} \qquad (C8)$$

substituting the value of Q in (C8):

$$\left[\frac{1}{A_G E_G (rx_G - rx_N)} - \frac{P}{A_G E_G} - \frac{P(rx_G - rx_N)^2}{E_G I_G}\right]$$

$$\times (1 - \nu_G^2) = \left[\frac{P}{A_N E_N} - \frac{1}{A_N E_N (rx_G - rx_N)}\right](1 - \nu_N^2) \qquad (C9)$$

Solving for P:

$$P = \frac{I_G(1 - \nu_G^2)E_N A_N + (1 - \nu_N^2)E_G A_G}{(rx_G - rx_N)\left\{E_N A_N\left[I_G + A_G(rx_G - rx_N)^2\right](1 - \nu_G^2) + E_G A_G I_G(1 - \nu_N^2)\right\}} \qquad (C10)$$

With reference to figure 27 the total uniform axial strain is:

$$\epsilon_{z,tot} = \epsilon_{z,G} - \epsilon_{z,N} \qquad (C11)$$

by similar triangles:

$$\frac{\epsilon_{z,tot}}{rx_G - rx_N} = - \frac{\epsilon_{z,N}}{r_c - rx_N} \quad \text{or} \quad r_c = rx_N - \frac{\epsilon_{z,N}(rx_G - rx_N)}{\epsilon_{z,tot}} \qquad (C12)$$

Substituting (C4), (C5), (C6), (C10) into (C12) and simplifying:

$$r_c = rx_N + \frac{(1 - \nu_N^2)A_G E_G (rx_G - rx_N)}{A_N E_N (1 - \nu_G^2) + A_G E_G (1 - \nu_N^2)} \tag{C13}$$

r_c is evaluated at each station along the length.

Equivalent Flexural Rigidity

Equivalent flexural rigidity D_{eq} is defined as the flexural rigidity of a sector of a cylinder which will produce a strain at a point on a sector equal to the strain obtained by the flexural rigidity of a composite section.

Substituting (C4) and (C10) into the rhs of (C8)

$$\epsilon_{z,N} = - \frac{(1 - \nu_N^2)(1 - \nu_G^2)A_G(rx_G - rx_N)}{(1 - \nu_G^2)E_N A_N \left[I_G + A_G(rx_G - rx_N)^2\right] + (1 - \nu_N^2)E_G I_G A_G} \tag{C14}$$

From figure 27, the strain $\epsilon_{z,N}$ can be defined as

$$- \epsilon_{z,N} = \theta(r_c - rx_N) = \frac{M1(r_c - rx_N)(1 - \nu_{eq}^2)}{E_{eq} I_{tot}} = \frac{M1(r_c - rx_N)}{D_{eq}} \tag{C15}$$

Substituting (C14) into (C15) and rearranging, D_{eq} is

$$D_{eq} = \frac{E_{eq} I_{tot}}{(1 - \nu_{eq}^2)}$$

$$= \frac{(r_c - rx_N)\left\{(1 - \nu_G^2)E_N A_N \left[I_G + A_G(rx_G - rx_N)^2\right] + (1 - \nu_N^2)E_G I_G A_G\right\}}{(1 - \nu_N^2)(1 - \nu_G^2)A_G(rx_G - rx_N)} \tag{C16}$$

D_{eq} is evaluated at each station along the length.

Spring Constant K of a Sector of a Composite Cylinder

To use elastic foundation theory a spring constant must be derived. Figure 28 shows a sector of a composite cylinder with a circumferential cut in equilibrium under a shrink-fit pressure load p_s, a pressure force p_c to restore compatibility, and a uniform pressure force p_a which is present due to the cut. Deflection compatibility between a and b is established using Lame's equations from reference 3, page 240 for deformations symmetrical about an axis due to internal and external pressures.

Parts a and b make up sector G. At r_j the deflections of a and N are equal, therefore

$$u_{a,j} = u_{N,j} \tag{C17}$$

or:

$$\left(\frac{1 - \nu_G}{E_G}\right)\left[\frac{r_j^2 p_s - r_c^2(p_a - p_c)}{(r_c^2 - r_j^2)}\right] r_j + \left(\frac{1 + \nu_G}{E_G}\right)\left[\frac{r_j r_c^2(p_s - p_a + p_c)}{(r_c^2 - r_j^2)}\right]$$

$$= -\frac{r_j p_s}{E_N}\left(\frac{r_i^2 + r_j^2}{r_j^2 - r_i^2} - \nu_N\right) \tag{C18}$$

Solving for p_s

$$p_s = \frac{2E_N r_c^2(p_a - p_c)}{S} \tag{C19}$$

where:

$$S = E_N\left[r_j^2 + r_c^2 + \nu_G(r_c^2 - r_j^2)\right] + E_G(r_c^2 - r_j^2)\left(\frac{r_i^2 + r_j^2}{r_j^2 - r_i^2} - \nu_N\right) \tag{C20}$$

At r_c the deflection of a is:

$$u_{a,c} = \frac{2p_s r_j^2 r_c - r_c(p_a - p_c)\left[r_c^2(1 - \nu_G) + r_j^2(1 + \nu_G)\right]}{E_G(r_c^2 - r_j^2)} \tag{C21}$$

At r_c the deflection of B is:

$$u_{b,c} = - \frac{p_c r_c}{E_G} \left(\frac{r_c^2 + r_o^2}{r_o^2 - r_c^2} + \nu_G \right) \tag{C22}$$

Setting $u_{a,c} = u_{b,c}$ and solving for p_c:

$$p_c = p_a \left\{ \frac{R - \left[r_c^2 + r_j^2 - \nu_G (r_c^2 - r_j^2) \right] \cdot S}{R - 2r_c^2 \left(\frac{r_o^2 - r_j^2}{r_o^2 - r_c^2} \right) \cdot S} \right\} \tag{C23}$$

where

$$R - 4r_j^2 r_c^2 E_N \tag{C24}$$

Setting the deflection of B at r_c to unity, substituting equation (C23) into (C22), solve for p_a to obtain the spring constant K which is equal to p_a

$$K = p_a = \frac{E_G}{r_c} \left[\frac{r_o^2 - r_c^2}{r_o^2 + r_c^2 + \nu_G (r_o^2 - r_c^2)} \right] \left\{ \frac{R - 2r_c^2 \left(\frac{r_o^2 - r_j^2}{r_o^2 - r_c^2} \right) \cdot S}{R - \left[r_c^2 + r_j^2 - \nu_G (r_c^2 - r_j^2) \right] \cdot S} \right\} \tag{C25}$$

K is evaluated at each station along the length.

Compensation for Use of a Thin Shell Theory on a Thick Shell Model

By using a method of solution based on the theory of beams on elastic foundation a thin shell analysis ($r/t > 10$) is implied, however, the mathematical model to be analyzed is physically a thick shell ($r/t < 2$). Coefficients will be derived below to be applied to the thin shell analysis radial displacement at r_c of the composite sector to obtain thick shell analysis displacements at various other radii (r_o, r_j, and r_i).

Lame's thick shell equations used previously in the calculation of a spring constant (eq. (C18)) will be used to derive a compensating coefficient H which is defined as a ratio of a radial displacement at various radii to the displacement of the sector at the neutral axis r_c:

$$H = \frac{u}{u_c} \tag{C26}$$

The displacement at r_c due to pressure p_c is obtained from equation (C22)

$$u_c = \frac{(-p_c)r_c\left[r_o^2 + r_c^2 + \nu_G(r_o^2 - r_c^2)\right]}{E_G(r_o^2 - r_c^2)} \tag{C27}$$

This radial displacement at r_o due to p_c is obtained from reference 3:

$$u_o = \frac{(1 - \nu_G)\left[r_c^2 r_o(-p_c)\right]}{E_G(r_o^2 - r_c^2)} + \frac{(1 + \nu_G)\left[r_c^2 r_o^2(-p_c)\right]}{E_G(r_o^2 - r_c^2)r_o} = \frac{2r_c^2 r_o(-p_c)}{E_G(r_o^2 - r_c^2)} \tag{C28}$$

Substituting (C27) and (C28) into (C26) and simplifying, the coefficient at r_o is:

$$H_1 = \frac{2r_o r_c}{r_o^2 + r_c^2 + \nu_G(r_o^2 - r_c^2)} \tag{C29}$$

The displacement of the lining at radius r_i due to external pressure p_s is:

$$u_i = \frac{(1 - \nu_N)(-r_i r_j^2 p_s)}{E_N(r_j^2 - r_i^2)} + \frac{(1 + \nu_N)(-r_i^2 r_j^2 p_s}{E_N(r_j^2 - r_i^2)r_i} = -\frac{2r_i r_j^2 p_s}{E_N(r_j^2 - r_i^2)} \tag{C30}$$

The radial displacement of r_c due to external pressure $p_a - p_c$ and an internal pressure p_s:

$$u_c = \frac{(1 - \nu_G)\left[r_j^2 p_s - r_c^2(p_a - p_c)\right]r_c}{E_G(r_c^2 - r_j^2)} + \frac{(1 + \nu_G)r_j^2 r_c^2\left[p_s - (p_a - p_c)\right]}{E_G(r_c^2 - r_j^2)r_c}$$

$$= \frac{r_c\left\{2p_s r_j^2 - (p_a - p_c)\left[r_c^2 + r_j^2 - \nu_G(r_c^2 - r_j^2)\right]\right\}}{E_G(r_c^2 - r_j^2)} \tag{C31}$$

Substituting (C30) and (C31) into (C26), replacing p_s by equation (C19) the coefficient to obtain the motion at r_i is:

$$H_2 = \frac{-4r_c r_j^2 r_i E_G (r_c^2 - r_j^2)}{(r_j^2 - r_i^2)\left\{4E_N r_c^2 r_j^2 - \left[r_c^2 + r_j^2 - \nu_G(r_c^2 - r_j^2)\right]S\right\}} \tag{C32}$$

where S is defined by equation (C20). The displacement at the juncture radius r_j due to external pressure $(p_a - p_c)$ and an internal pressure of p_s:

$$u_j = \frac{(1 - \nu_G)\left[r_j^2 p_s - r_c^2(p_a - p_c)\right]r_j}{E_G(r_c^2 - r_j^2)} + \frac{(1 + \nu_G)r_j^2 r_c^2\left[p_s - (p_a - p_c)\right]}{E_G(r_c^2 - r_j^2)r_j}$$

$$= \frac{r_j\left\{p_s\left[r_j^2 + r_c^2 + \nu_G(r_c^2 - r_j^2)\right] - 2r_c^2(p_a - p_c)\right\}}{E_G(r_c^2 - r_j^2)} \tag{C33}$$

Substituting (C31) and (C33) into (C26) replacing p_s by equation (C19) the coefficient to obtain the motion at r_j is:

$$H_3 = \frac{2r_j r_c\left\{E_N\left[r_j^2 + r_c^2 + \nu_G(r_c^2 - r_j^2)\right] - S\right\}}{4r_j^2 r_c^2 E_N - \left[r_c^2 + r_j^2 - \nu_G(r_c^2 - r_j^2)\right]S} \tag{C34}$$

H_1, H_2, H_3 are evaluated at each station along the length.

Summary of Elastic Foundation Coefficients

The fuel element model is divided into m finite cylinder elements (fig. 9) of length l_m such that the parameter $\lambda l_m < \pi/4$. The factor λ as defined in reference 2, page 4, has been redefined for this analysis:

$$\lambda_m = \sqrt[4]{\frac{K_m}{4D_{eq,m}}} \tag{C35}$$

where

K_m = average of K_n and K_{n+1} of element m (eq. (C25))

$D_{eq,n}$ = average of D_{eq_n} and $D_{eq_{n+1}}$ of element m (eq. (C16))

The coefficients obtained from reference 2, pages 52 and 53 are

summarized below for use in determining displacements and rotations at both ends (stations) of element m.

For a finite beam on an elastic foundation (spring rate K_m) with free ends the displacements u at both end points, stations n and n + 1, respectively, due to a concentrated shear force V_n applied at end n are;

$$u_n = V_n B_{1,m} \tag{C36}$$

$$u_{n+1} = V_n B_{2,m} \tag{C37}$$

where

$$B_{1,m} = \left(\frac{\sinh \lambda l \cosh \lambda l - \sin \lambda l \cos \lambda l}{DEN}\right) 2\lambda \tag{C38}$$

$$B_{2,m} = \left(\frac{\sinh \lambda l \cos \lambda l - \sin \lambda l \cosh \lambda l}{DEN}\right) 2\lambda \tag{C39}$$

$$DEN = (\sinh^2 \lambda l - \sin^2 \lambda l) K_m \tag{C40}$$

The subscript m applied to λ and l have been deleted for clarity. Similarly the displacements u and rotations Φ due to a concentrated moment Me applied at end n are;

$$u_n = MeB_{3,m} \tag{C41}$$

$$u_{n+1} = MeB_{4,m} \tag{C42}$$

$$\Phi_n = MeB_{5,m} \tag{C43}$$

$$\Phi_{n+1} = MeB_{6,m} \tag{C44}$$

where

$$B_{3,m} = \left(\frac{\sinh^2 \lambda l + \sin^2 \lambda l}{DEN}\right) 2\lambda^2 \tag{C45}$$

$$B_{4,m} = \left(\frac{\sinh \lambda l \sin \lambda l}{DEN}\right) 4\lambda^2 \tag{C46}$$

$$B_{5,m} = \left(\frac{\sinh \lambda l \cosh \lambda l + \sin \lambda l \cos \lambda l}{DEN} \right) 4\lambda^3 \qquad (C47)$$

$$B_{6,m} = \left(\frac{\sinh \lambda l \cos \lambda l + \sin \lambda l \cosh \lambda l}{DEN} \right) 4\lambda^3 \qquad (C48)$$

The above coefficients are evaluated at each station n along the length.

REFERENCES

1. Clark, John S.: Analytical Comparison of Material Temperatures for Nuclear and Electrically Heated Nuclear Reactor Fuel Elements. NASA TM X-1180, 1965.

2. Hetenyi, M.: Beams on Elastic Foundation. University of Michigan Press, Ann Arbor, Michigan, 1938.

3. Timoshenko, S.: Strength of Materials, Volume 2, McGraw-Hill Book Company, Inc., Second Edition, 1941.

4. Timoshenko, S. and Goodier, J. N.: Theory of Elasticity. McGraw-Hill Book Company, Inc., 1951.

5. Schwarzkopf, P. and Kieffer, Richard: Refractory Hand Metals. MacMillan Company, 1953.

6. Anon.: The Industrial Graphite Engineering Handbook. Union Carbide Corporation, 1964.

7. Kolomvets, N. V.; Neshpar, V. S.; Samsonov, G. V. and Semenkovich, S. A.: Fhur. Tech., Figure 28, 2382-9 (1958).

8. The Thermal Properties of Thirteen Solid Materials to 5000° F or Their Destruction Temperatures. WADD TR 60-924, February 1962.

[redacted]

ANALYTICAL STUDY OF SOME THERMAL STRESSES IN A NUCLEAR ROCKET FUEL ELEMENT (U)

by Edward R. Hersman, Eugene J. Pleban, John S. Clark,
and Dennis P. Townsend

ABSTRACT

An alytical calculation was made to determine the approximate magnitude of thermal stresses in a nuclear rocket fuel element when heated either in the reactor or by electrical conduction. The analysis was confined to the elastic region. This limiation results in stress values which can be used only in a comparative way.

The study showed that very high stresses are induced into the surface coating of NbC as a result of the great dissimilarity in the mean coefficient of thermal expansion of the coating and the graphite body of the fuel element.

[redacted]

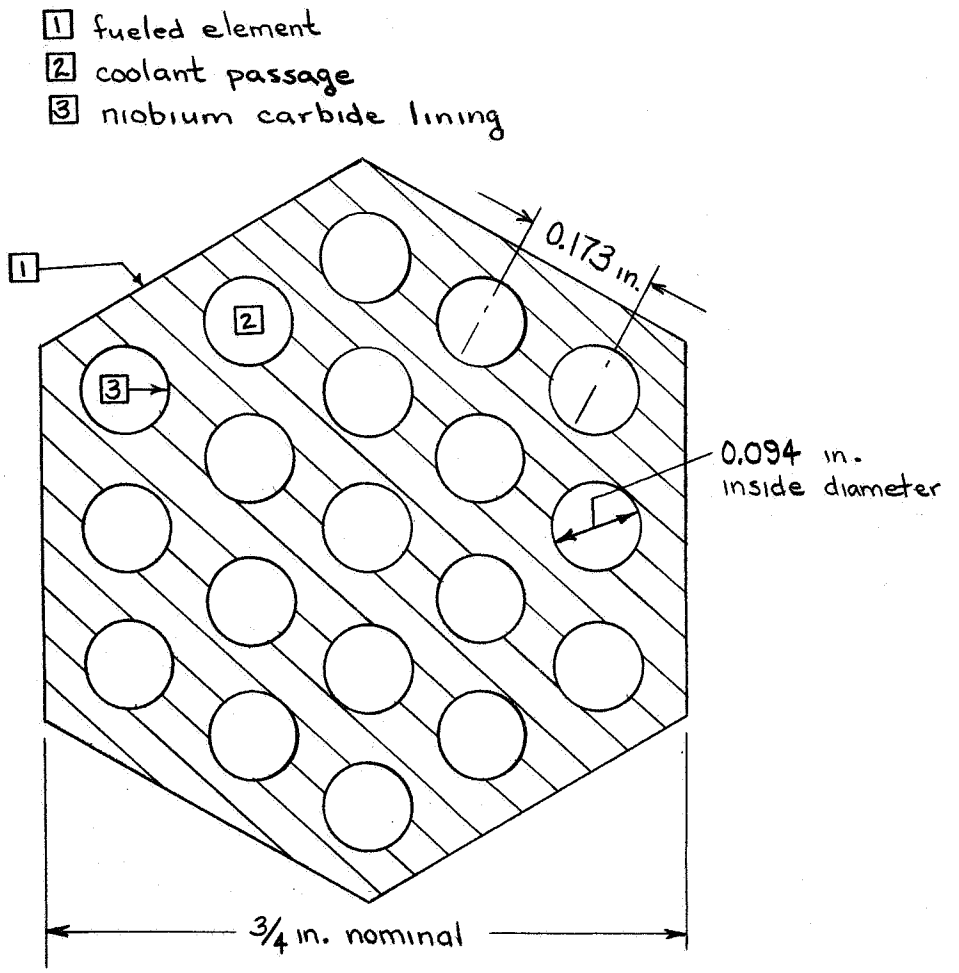

b) Cross-sectional view

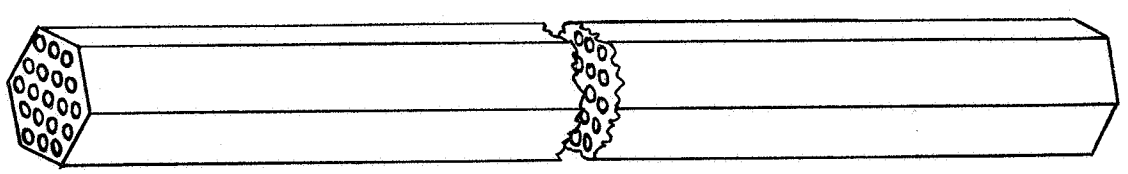

a) Schematic view

Figure 1.- Standard fuel element - 52 in. long - 3/4 in. hex

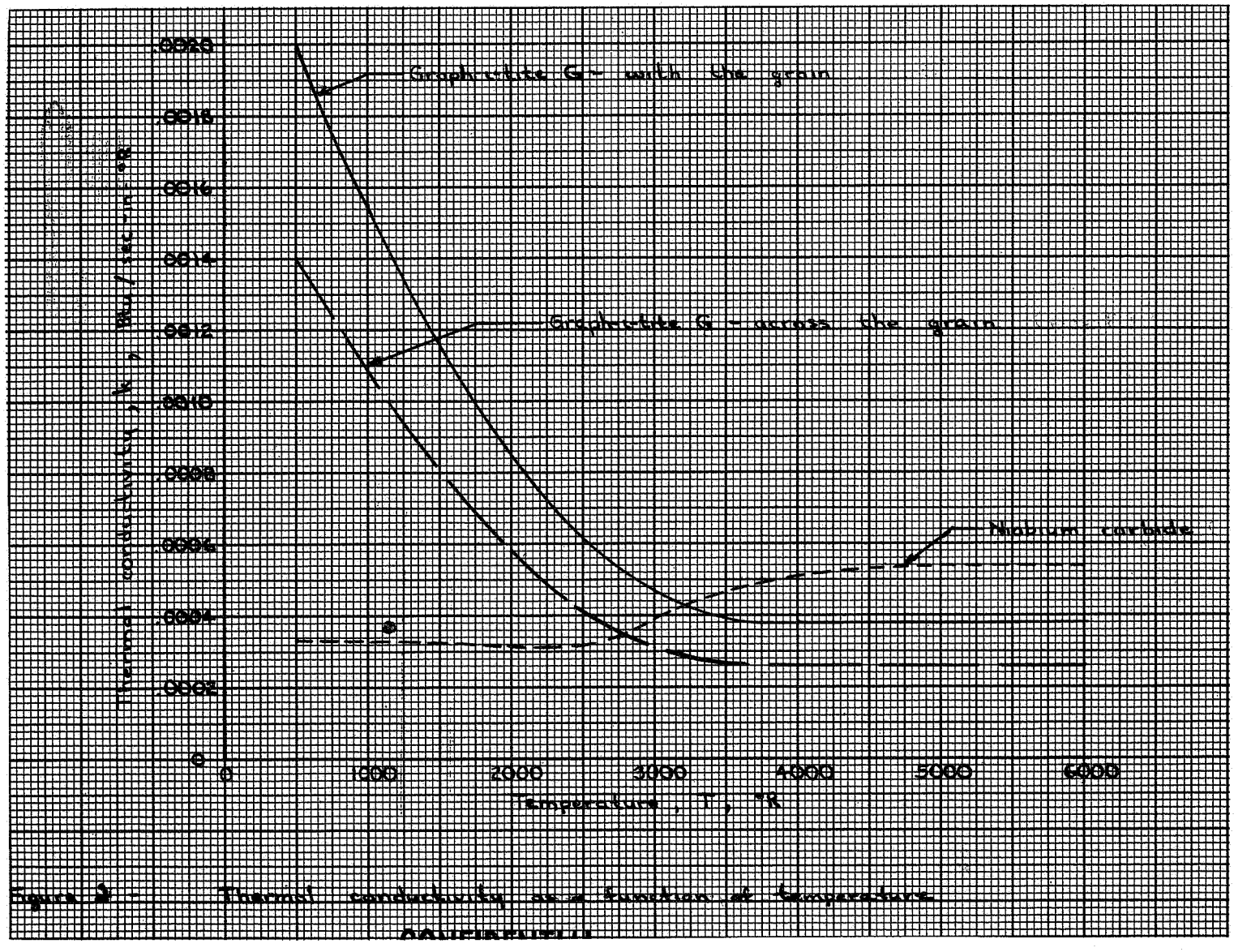

Figure 3. - Thermal conductivity as a function of temperature.

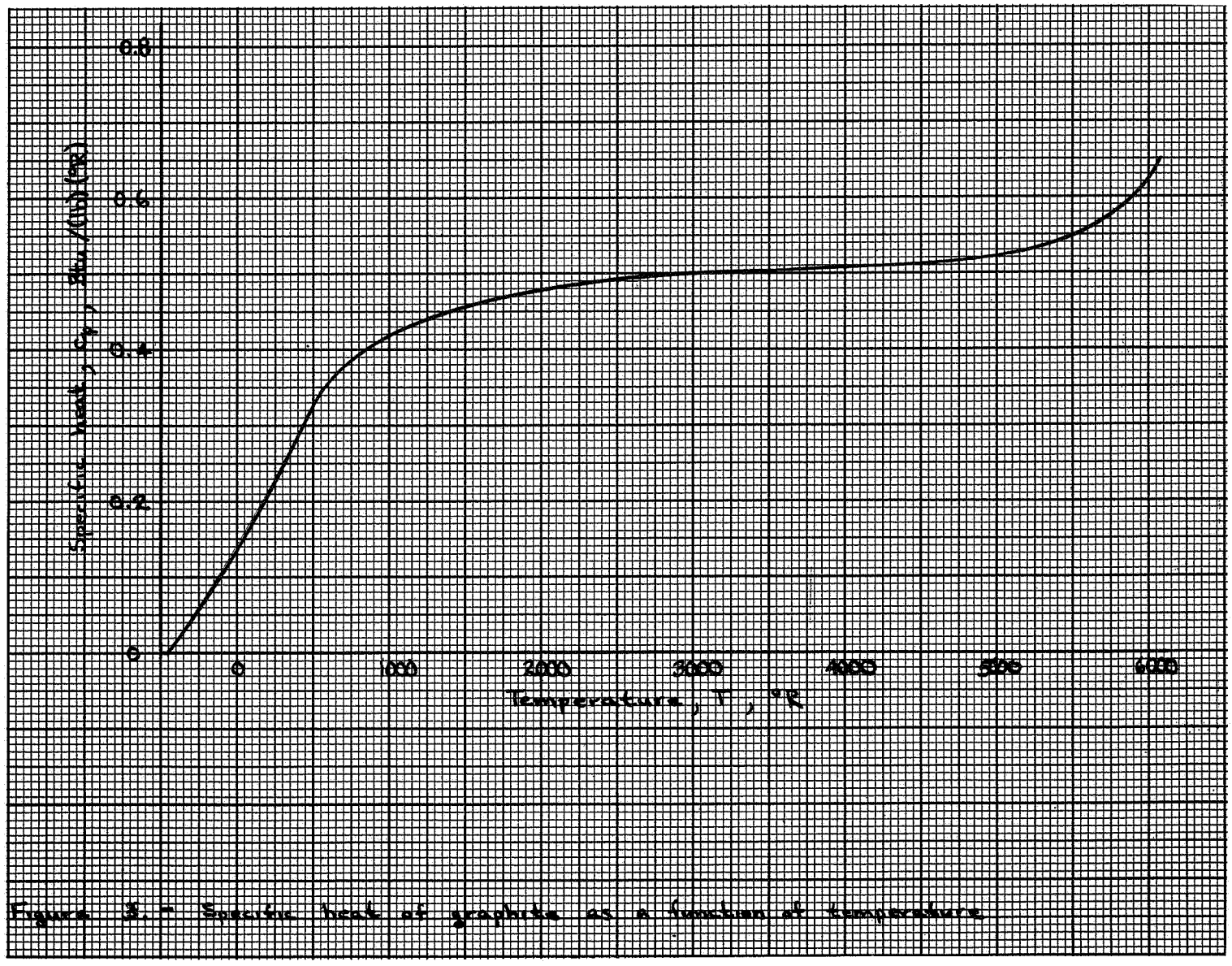

Figure 3. - Specific heat of graphite as a function of temperature.

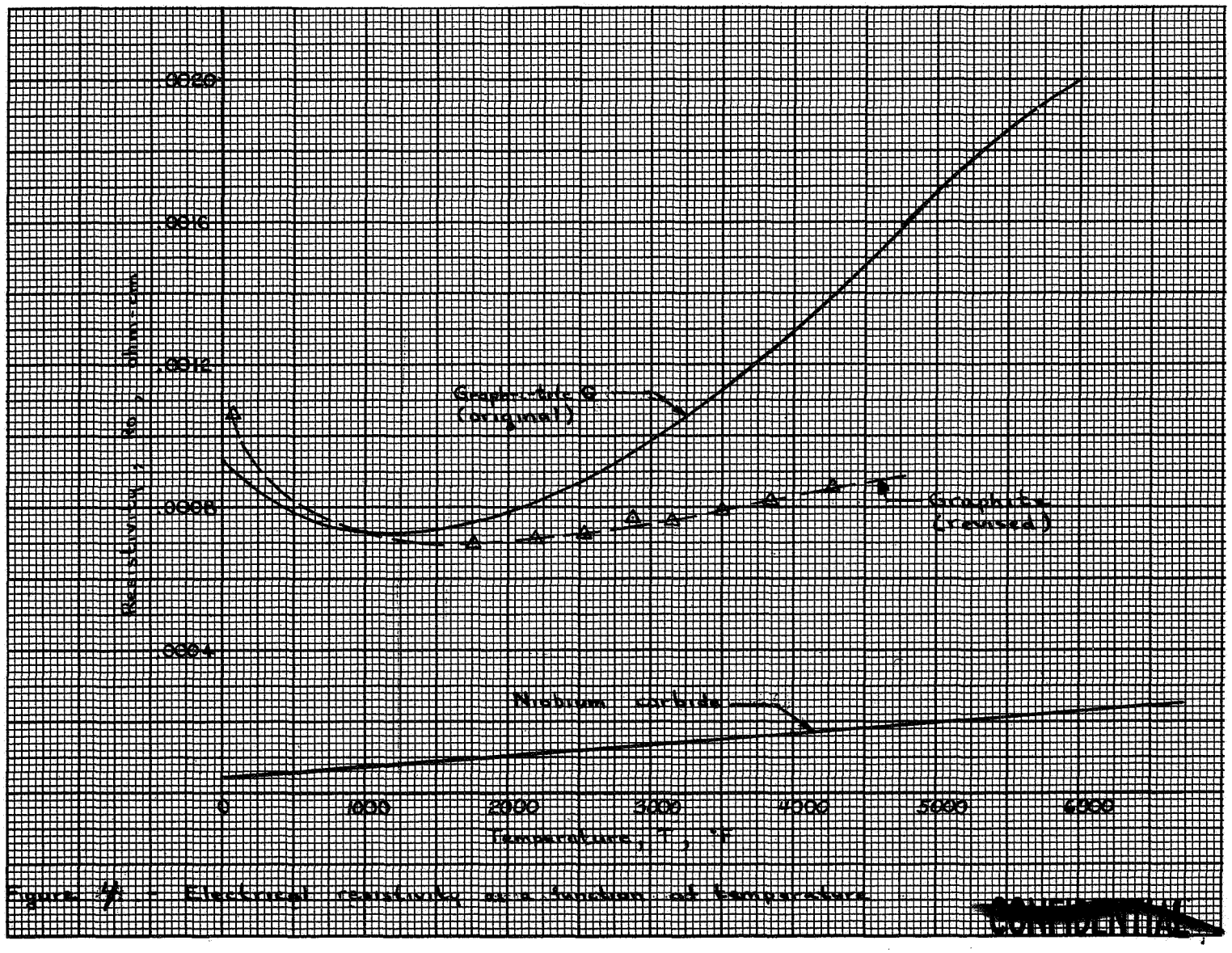

Figure 4 - Electrical resistivity as a function of temperature.

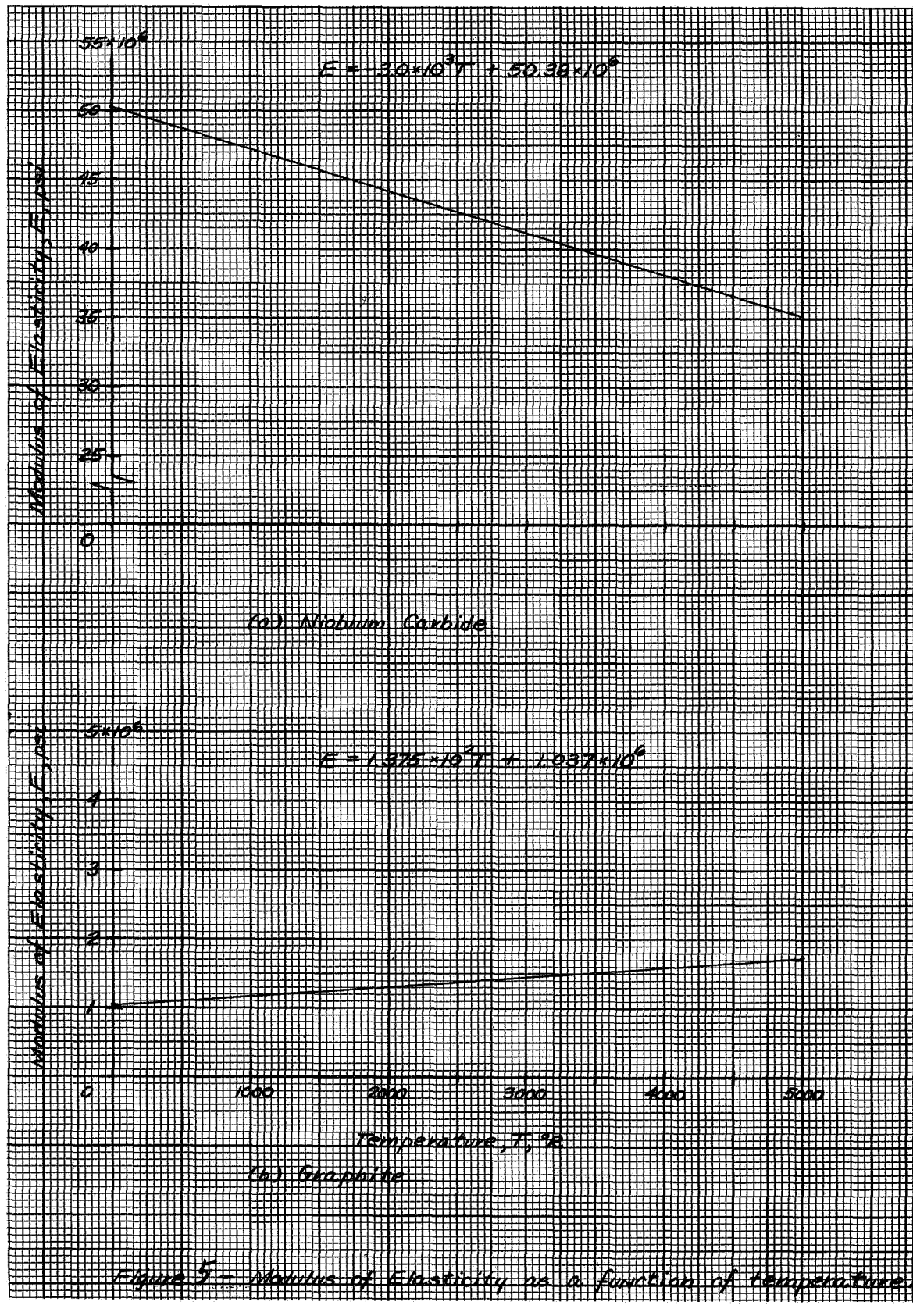

Figure 5 - Modulus of Elasticity as a function of temperature.

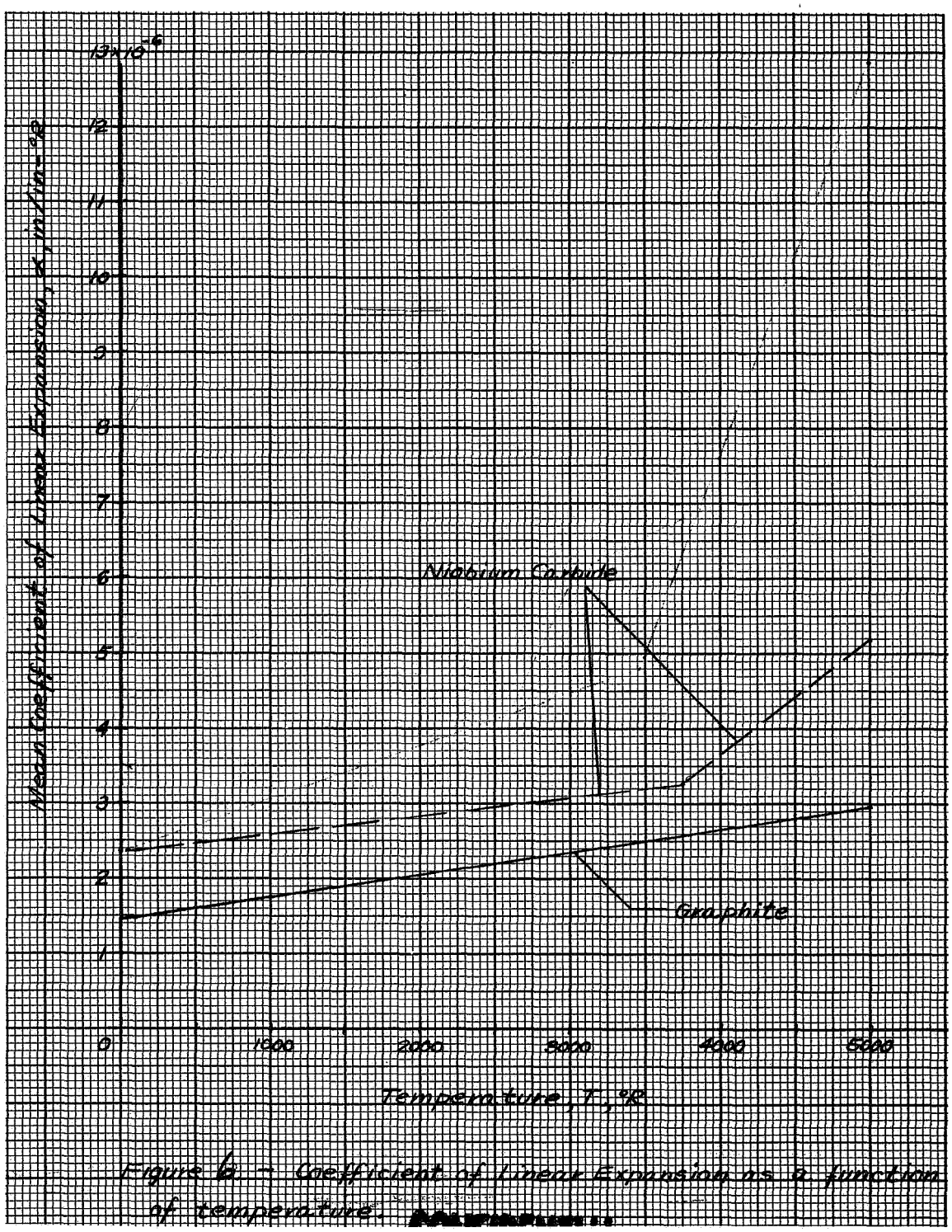

Figure 6 - Coefficient of Linear Expansion as a function of temperature.

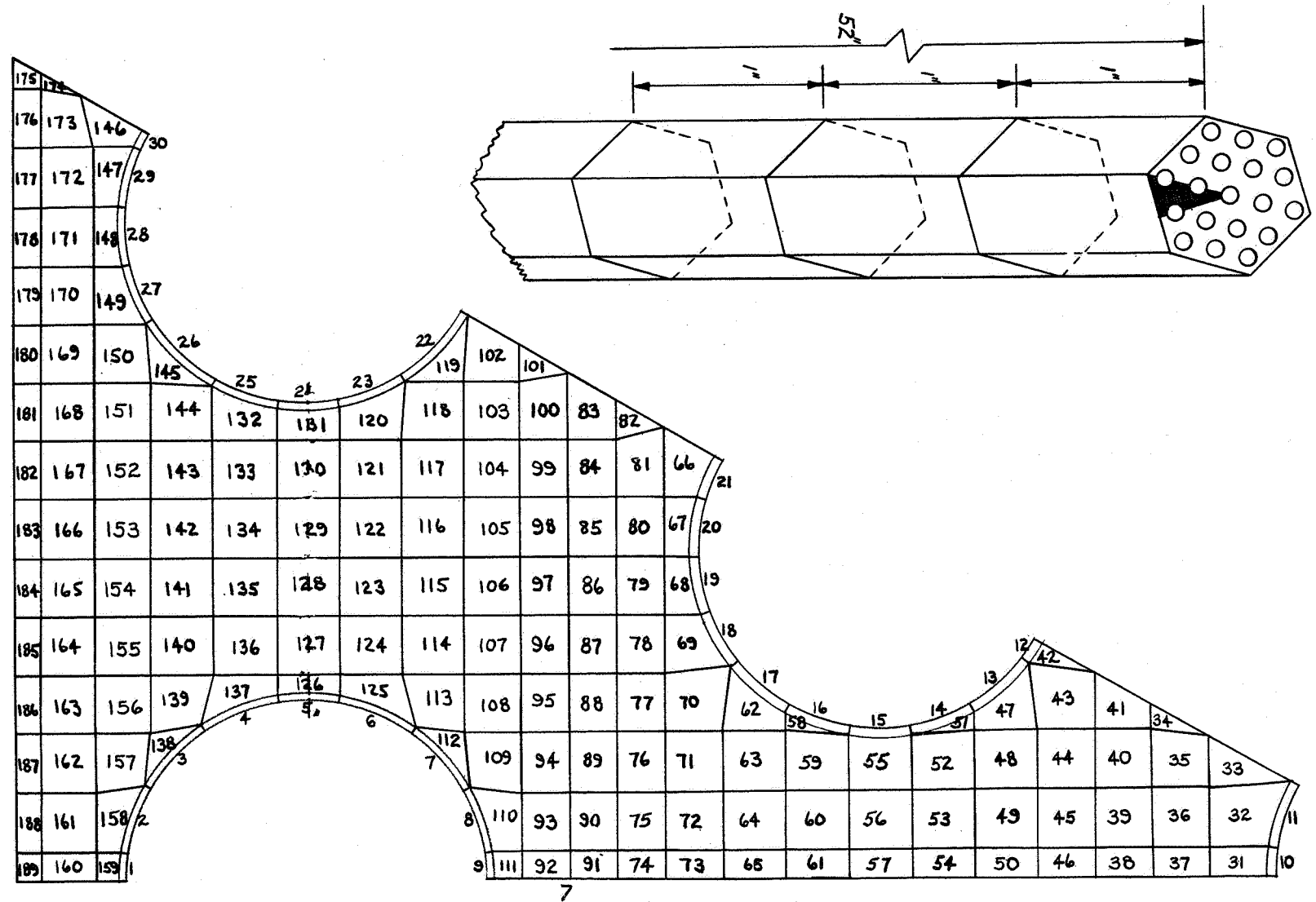

Figure 7.- Fuel element node description.

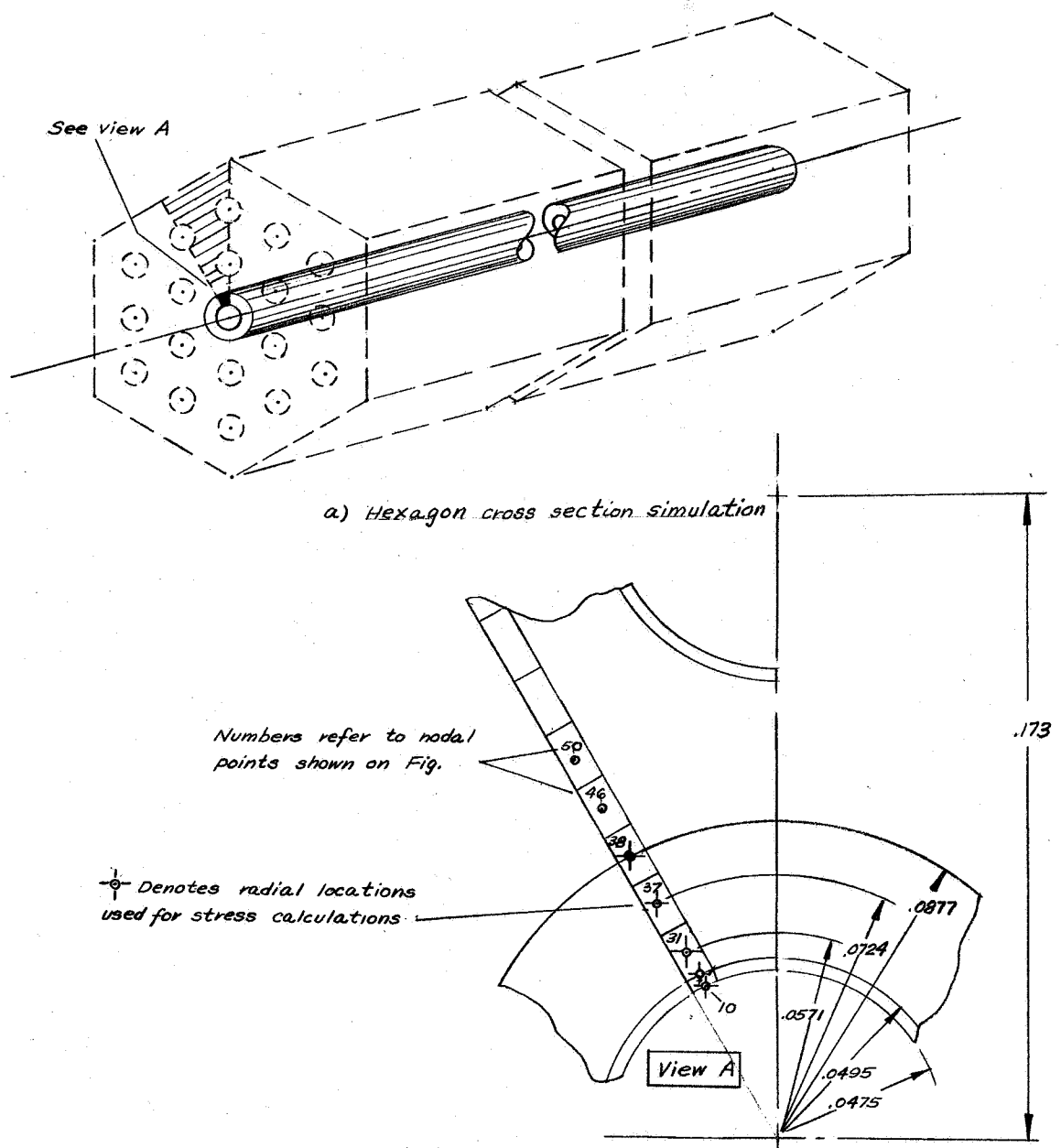

Figure 8 - Sketch of fuel element showing simplified cylindrical model used for stress calculations.

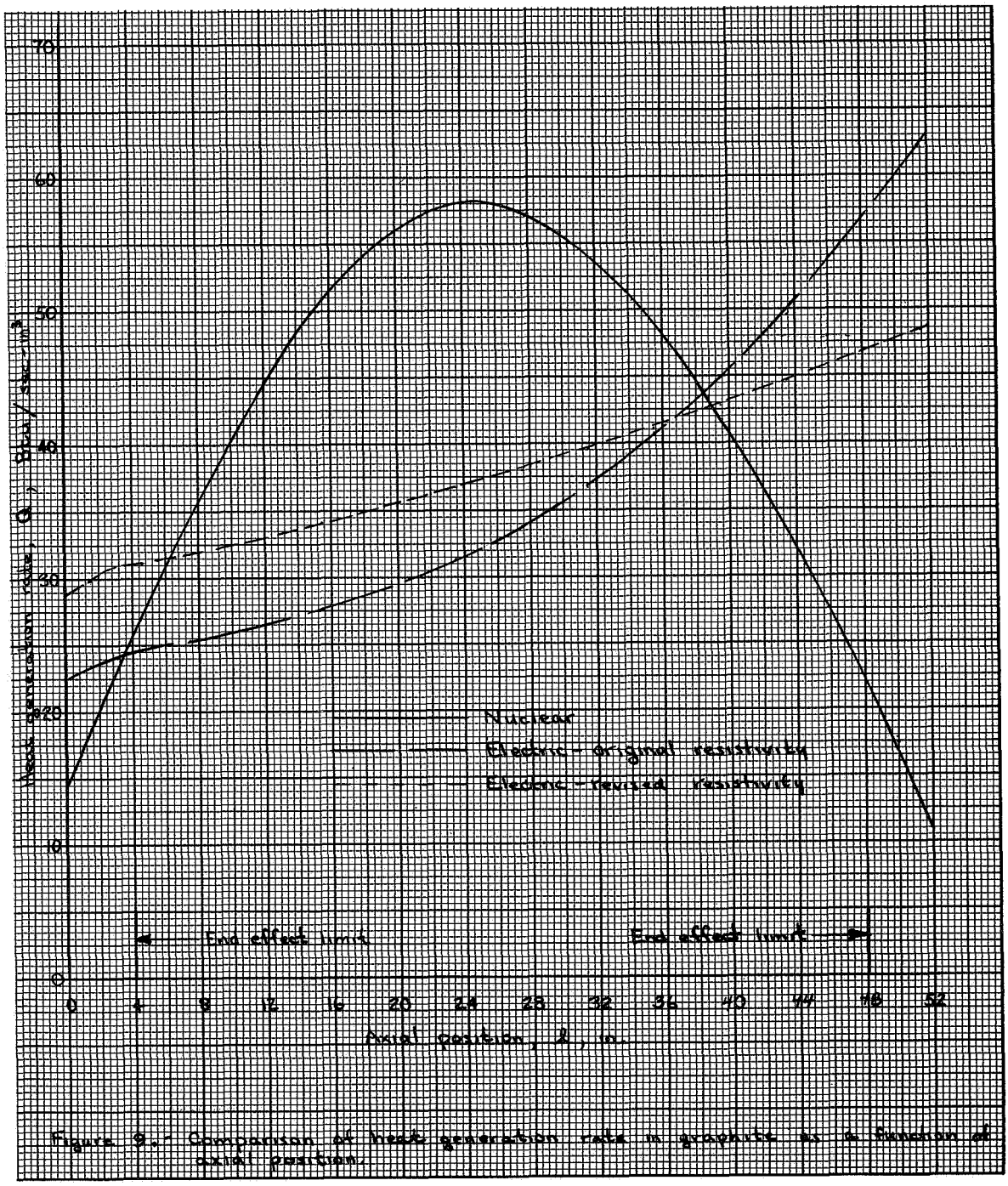

Figure 9.- Comparison of heat generation rate in graphite as a function of axial position.

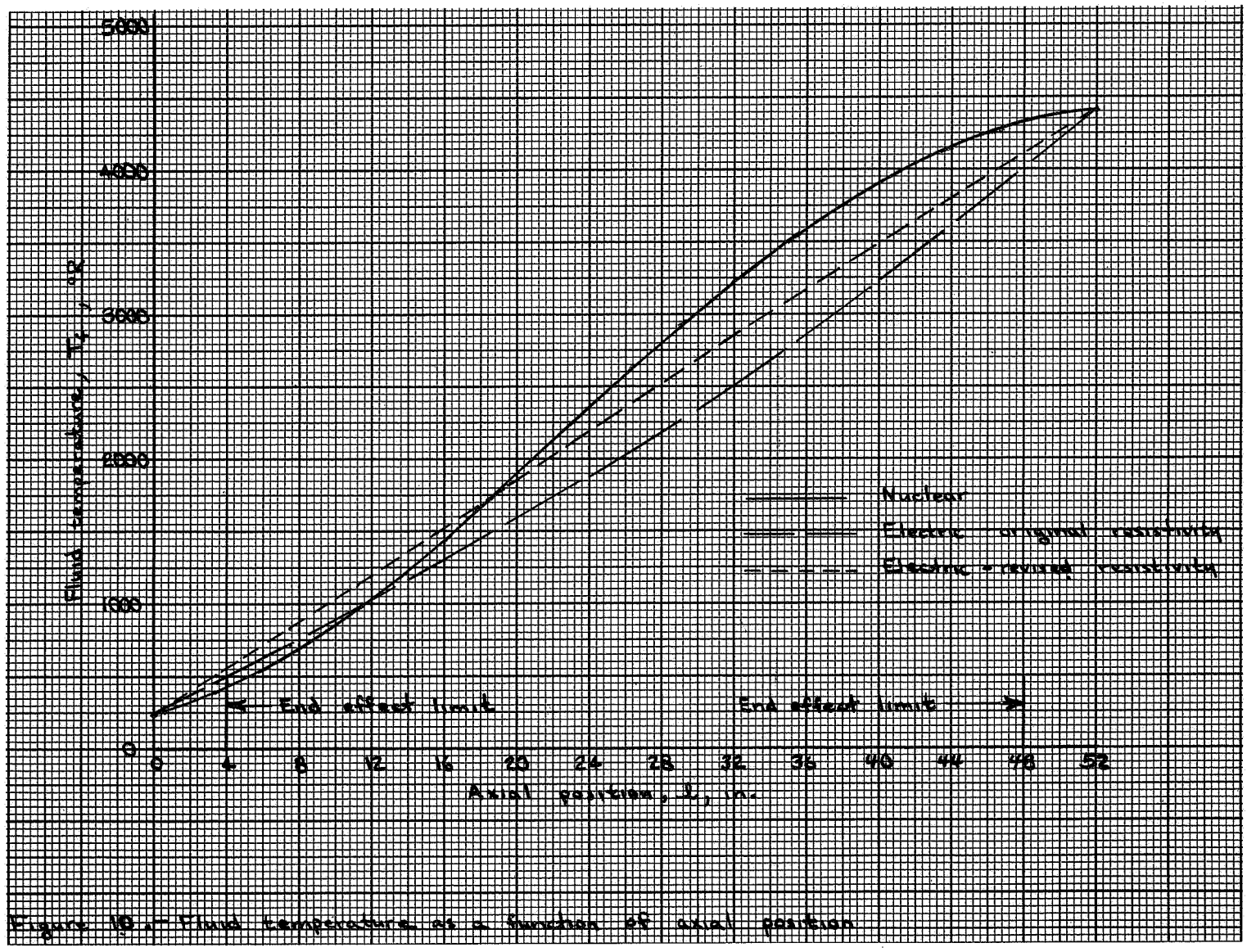

Figure 19.- Fluid temperature as a function of axial position

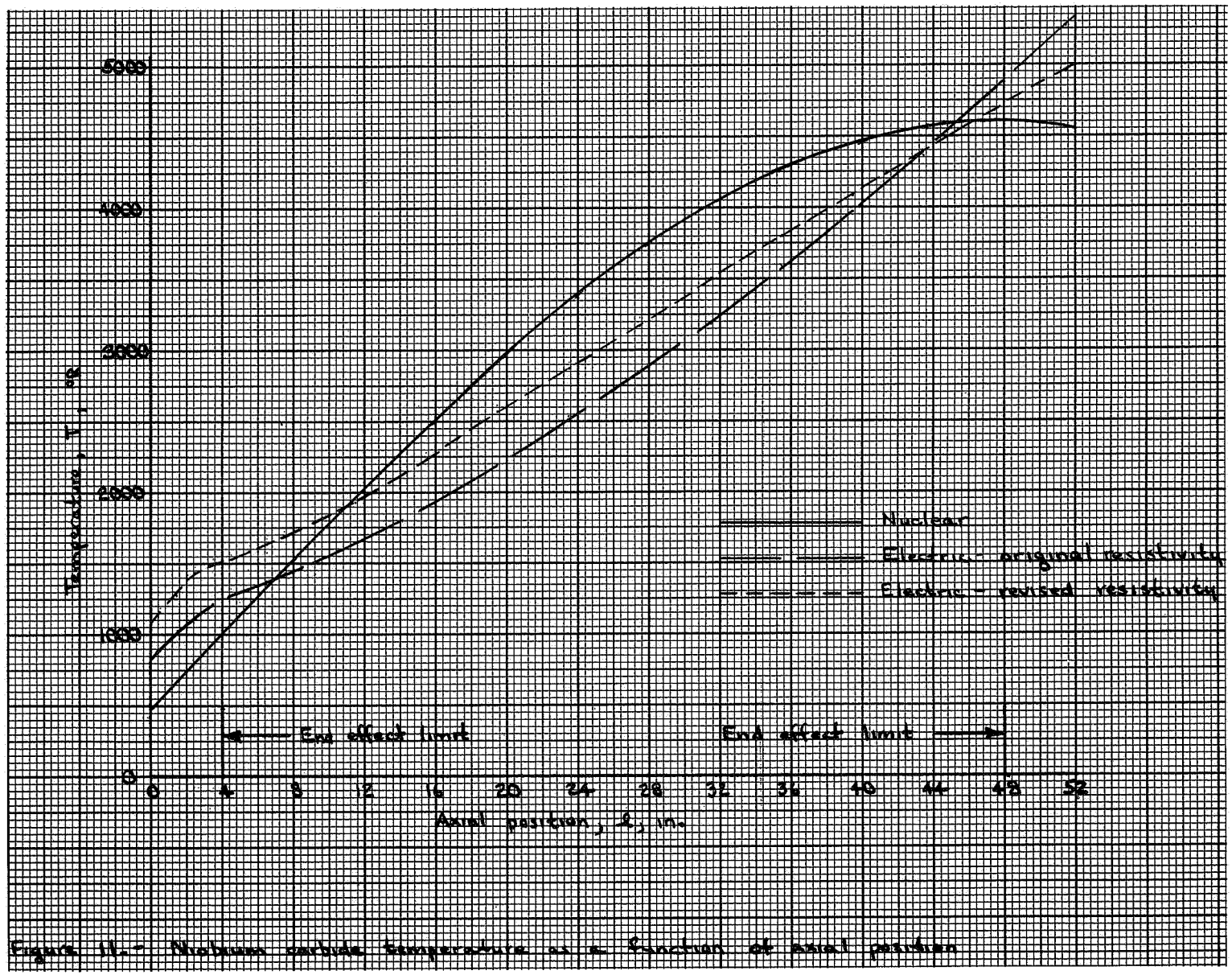

Figure 11.- Niobium carbide temperature as a function of axial position

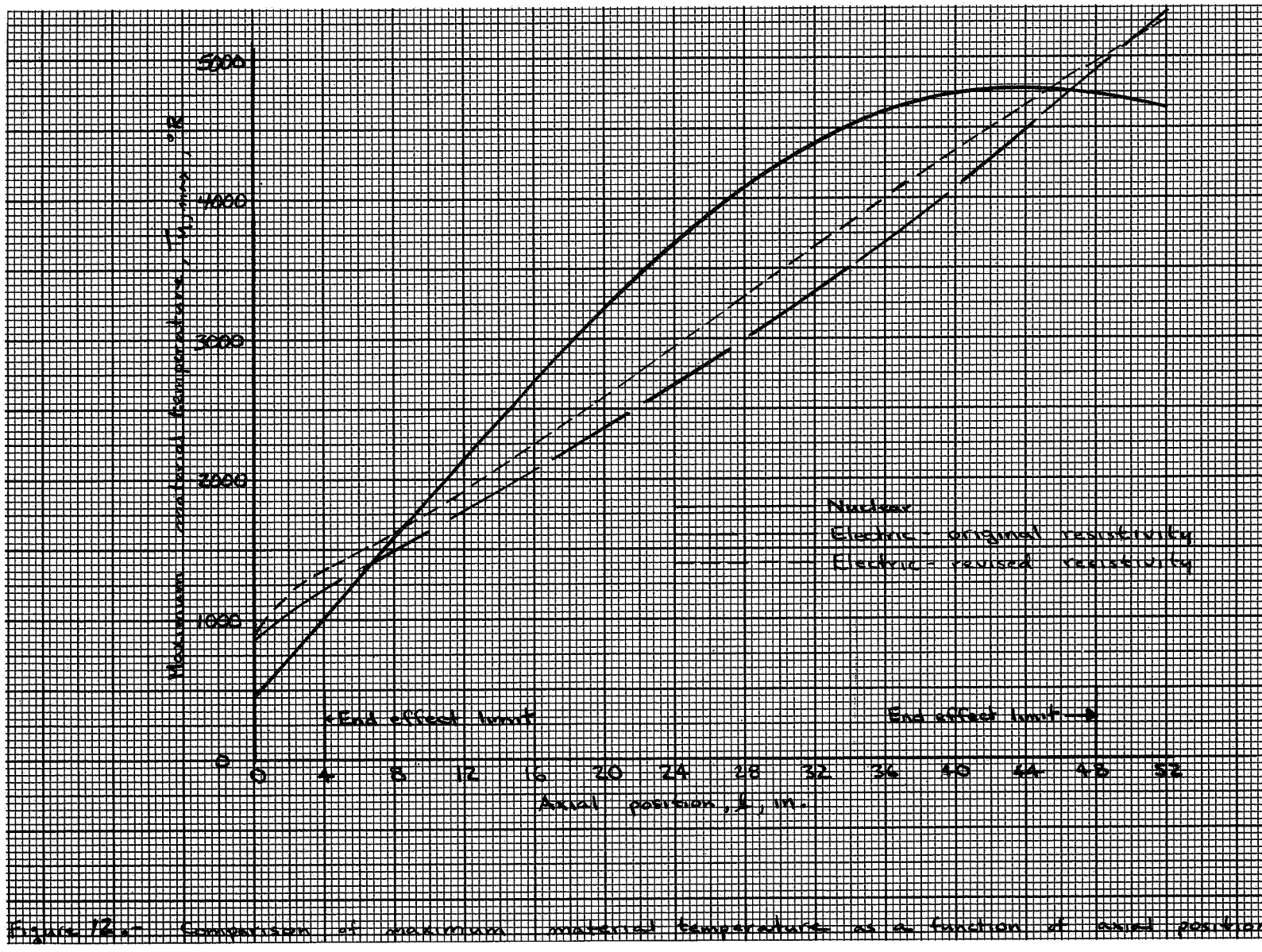

Figure 72.- Comparison of maximum material temperatures as a function of axial position

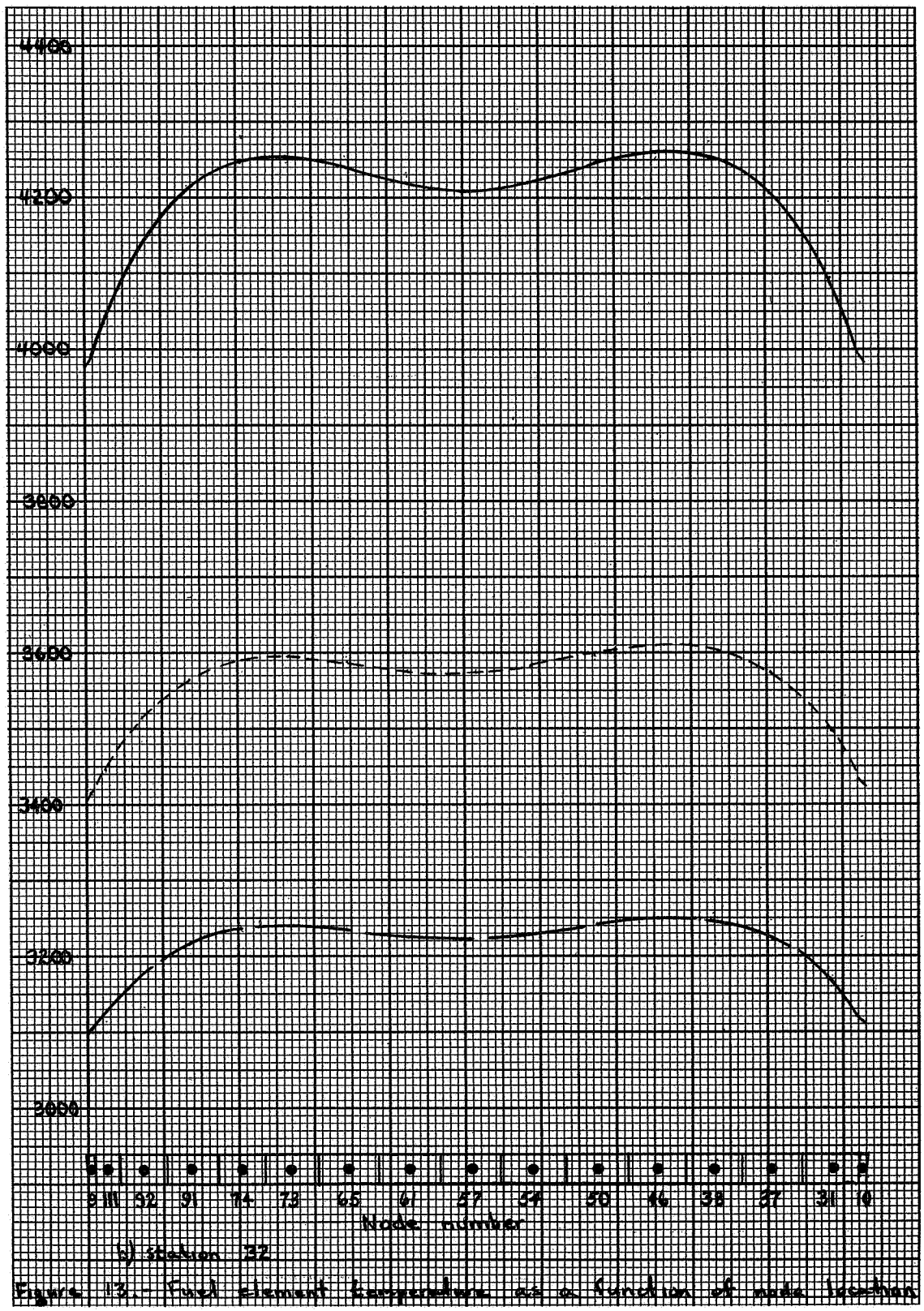

b) Section 32

Figure 13 - Fuel element temperatures as a function of node location

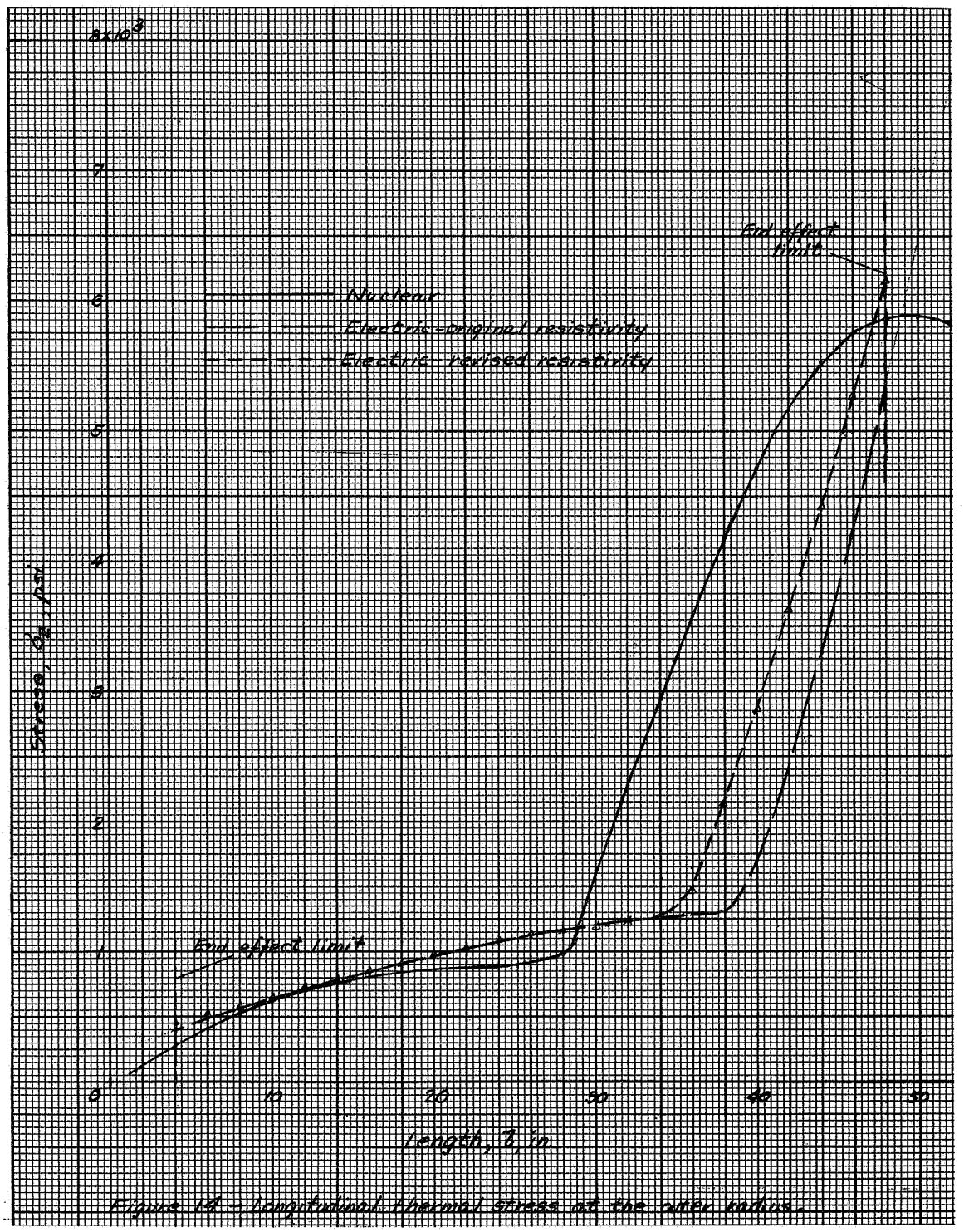

Figure 18 - Longitudinal thermal stress at the outer radius.

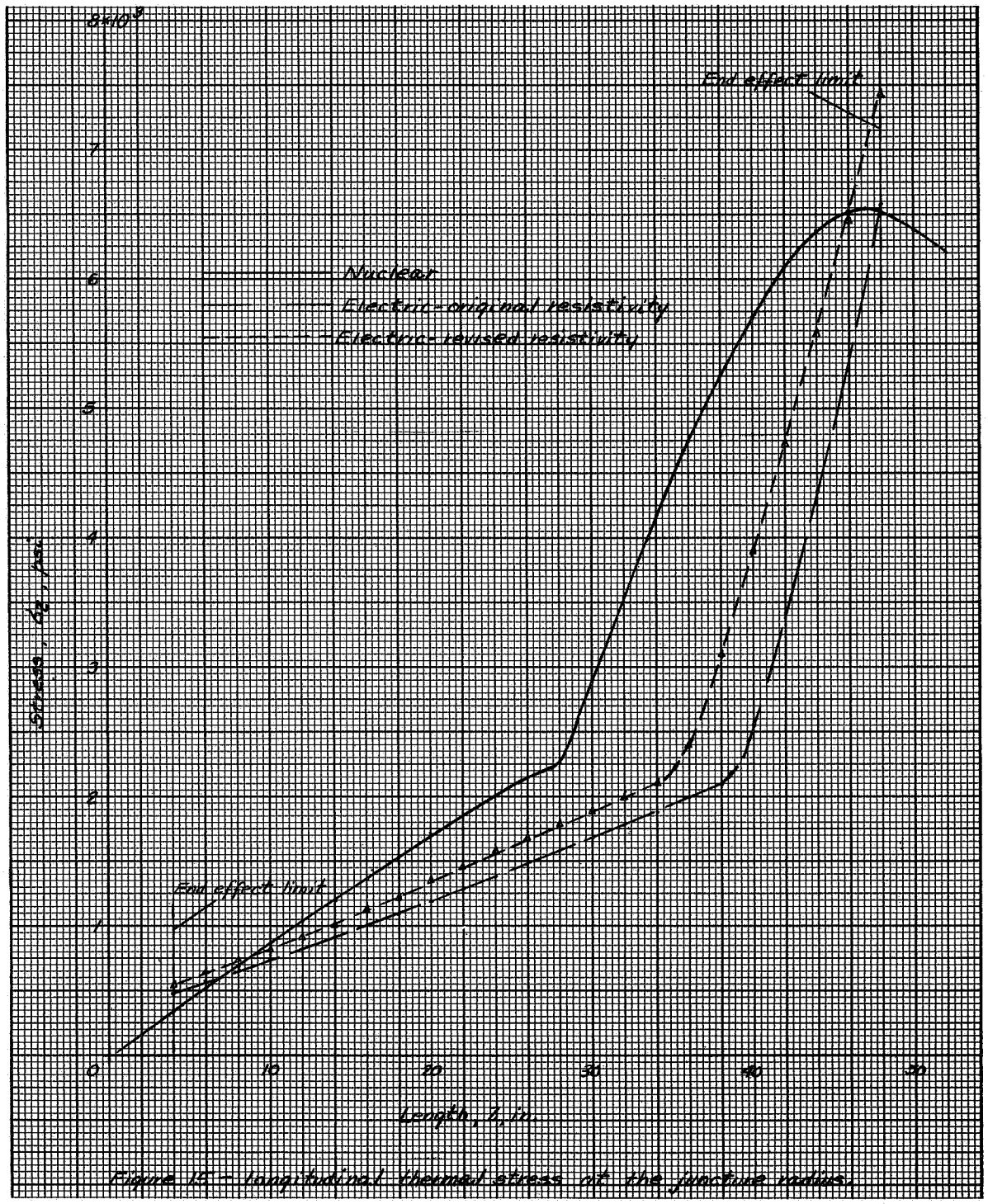

Figure 18 - Longitudinal thermal stress at the junction radius.

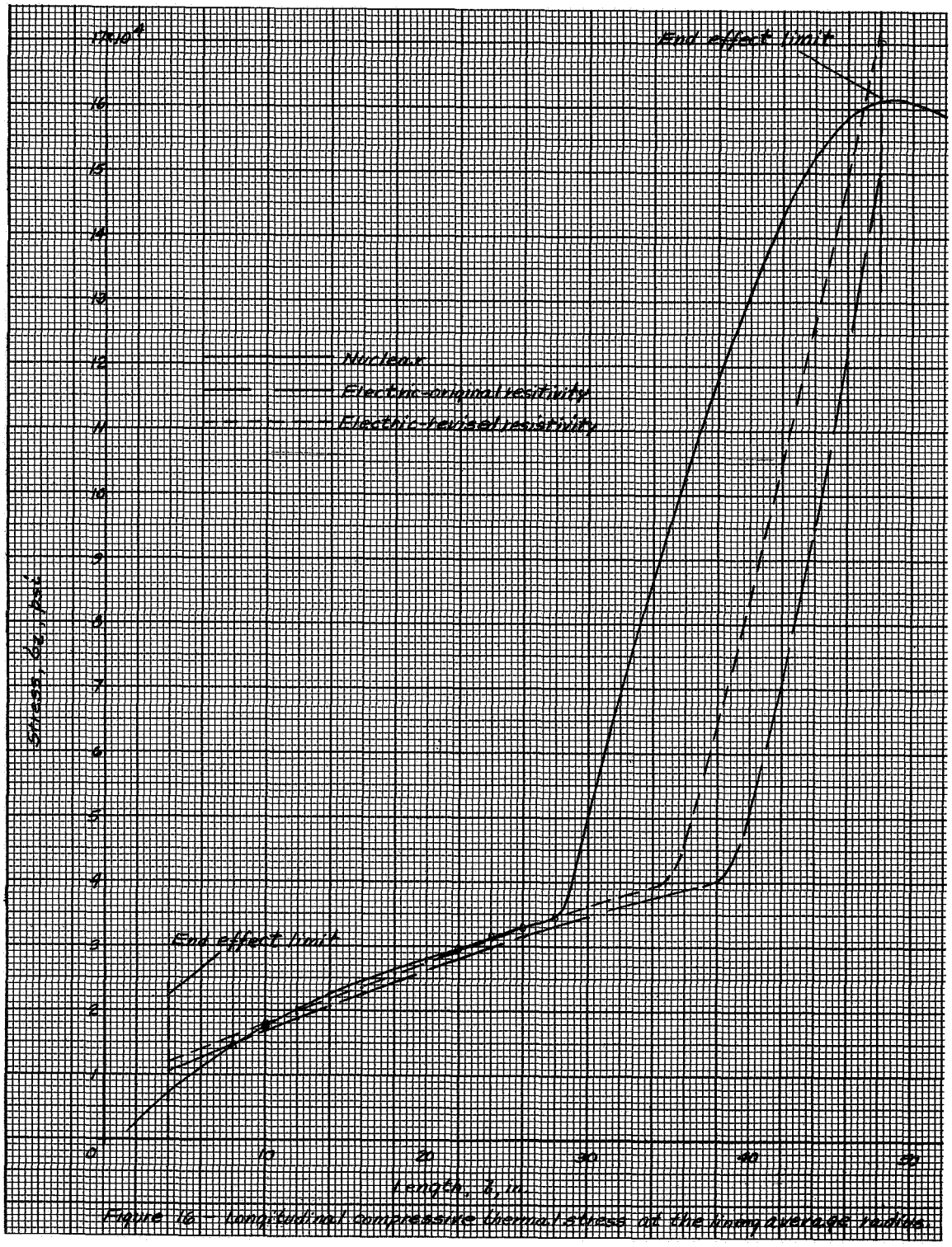

Figure 16 - Longitudinal compressive thermal stress at the long average radius.

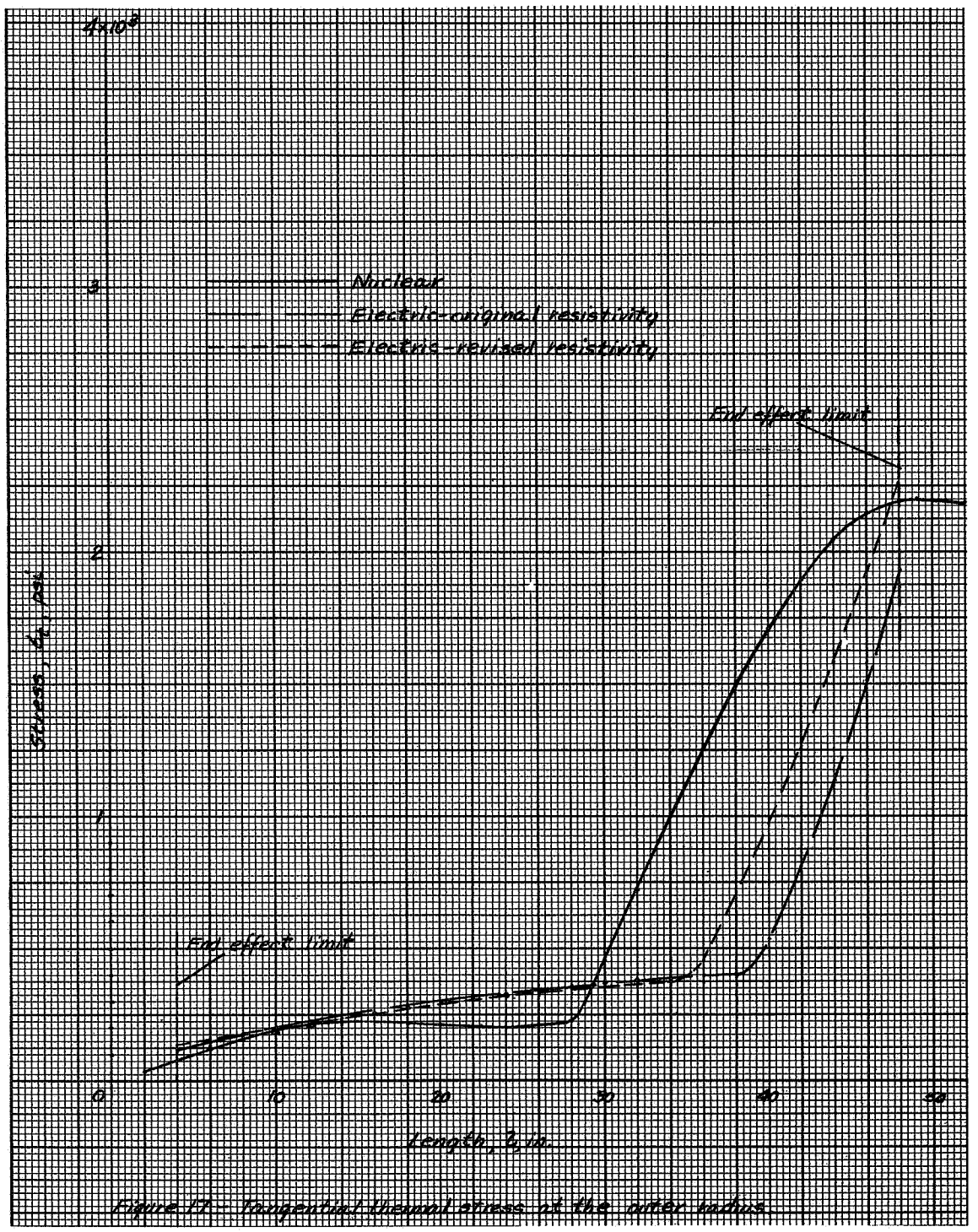

Figure 12 - Tangential thermal stress at the outer radius.

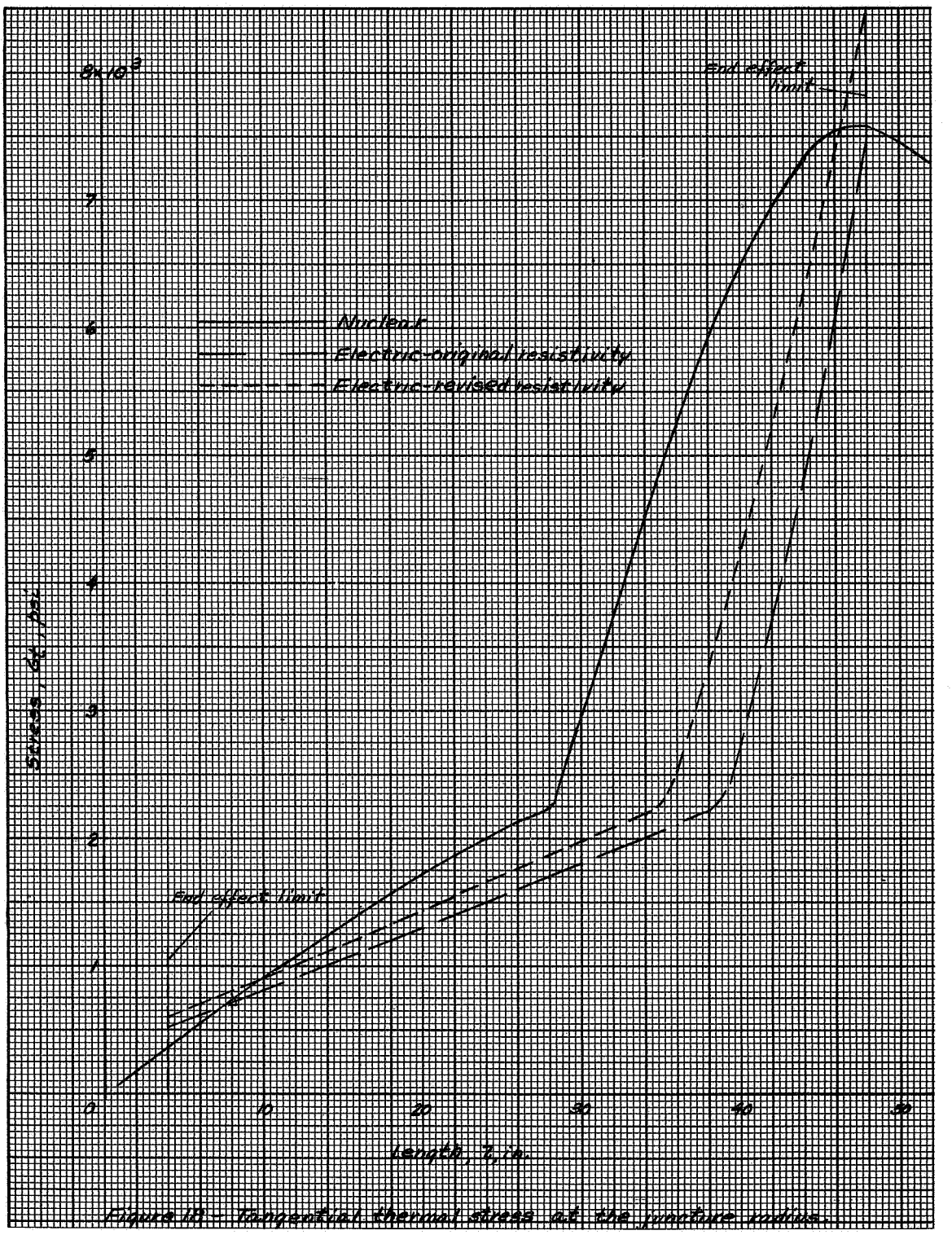

Figure 19 - Tangential thermal stress at the juncture radius.

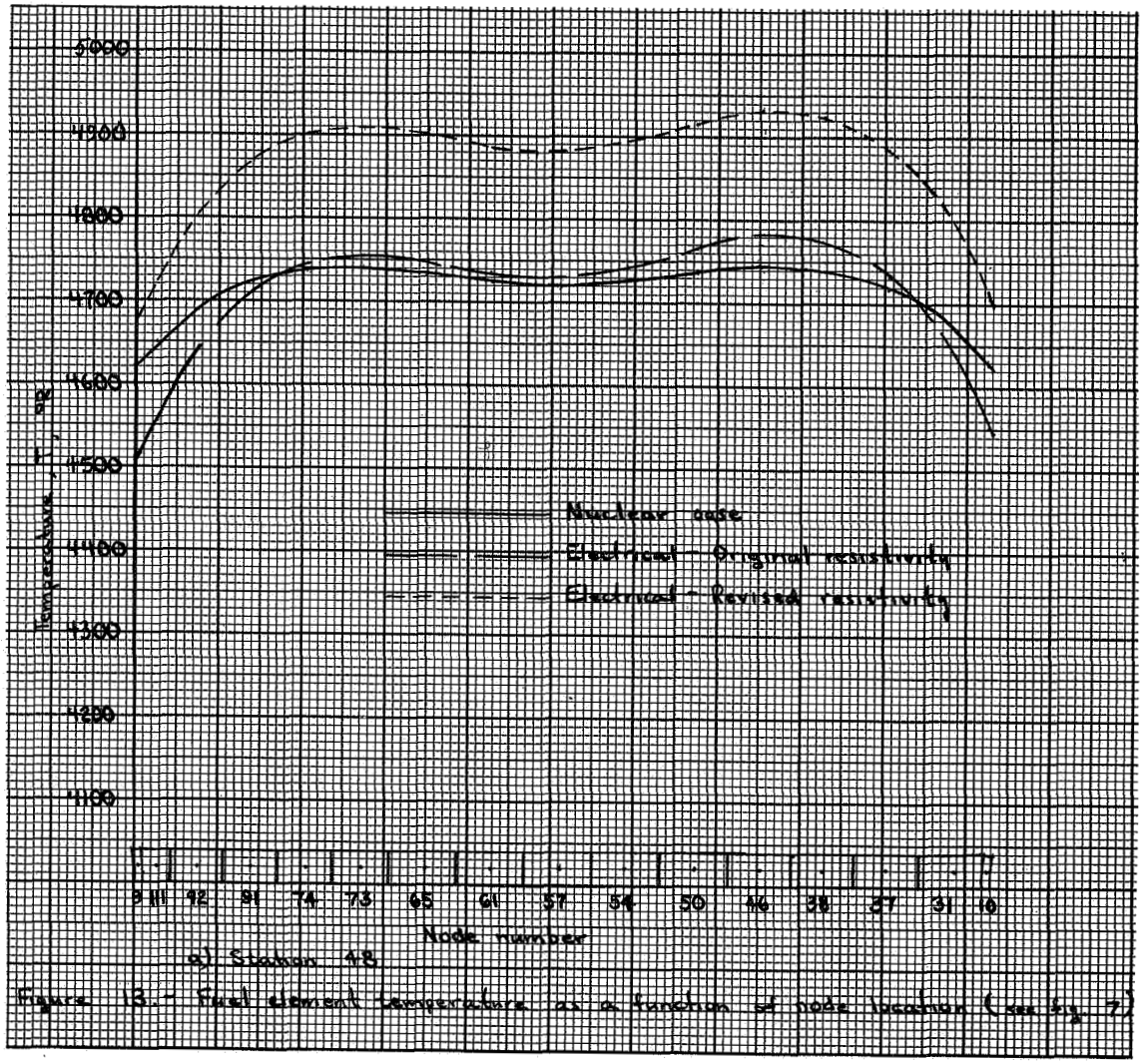

a) Station 48

Figure 18. - Fuel element temperature as a function of node location (see fig. 7)

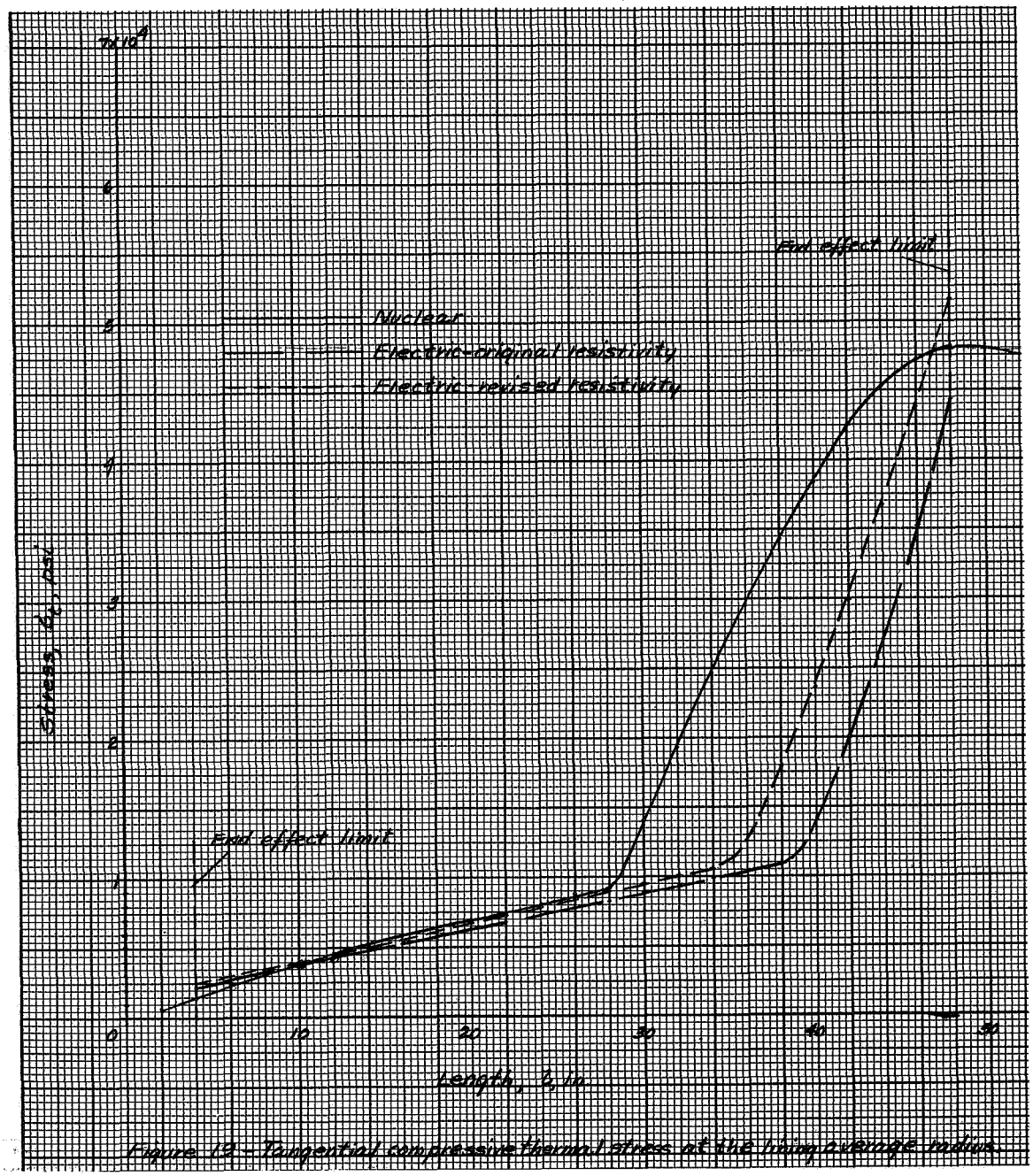

Figure 19 - Tangential compressive thermal stress at the bore average radius.

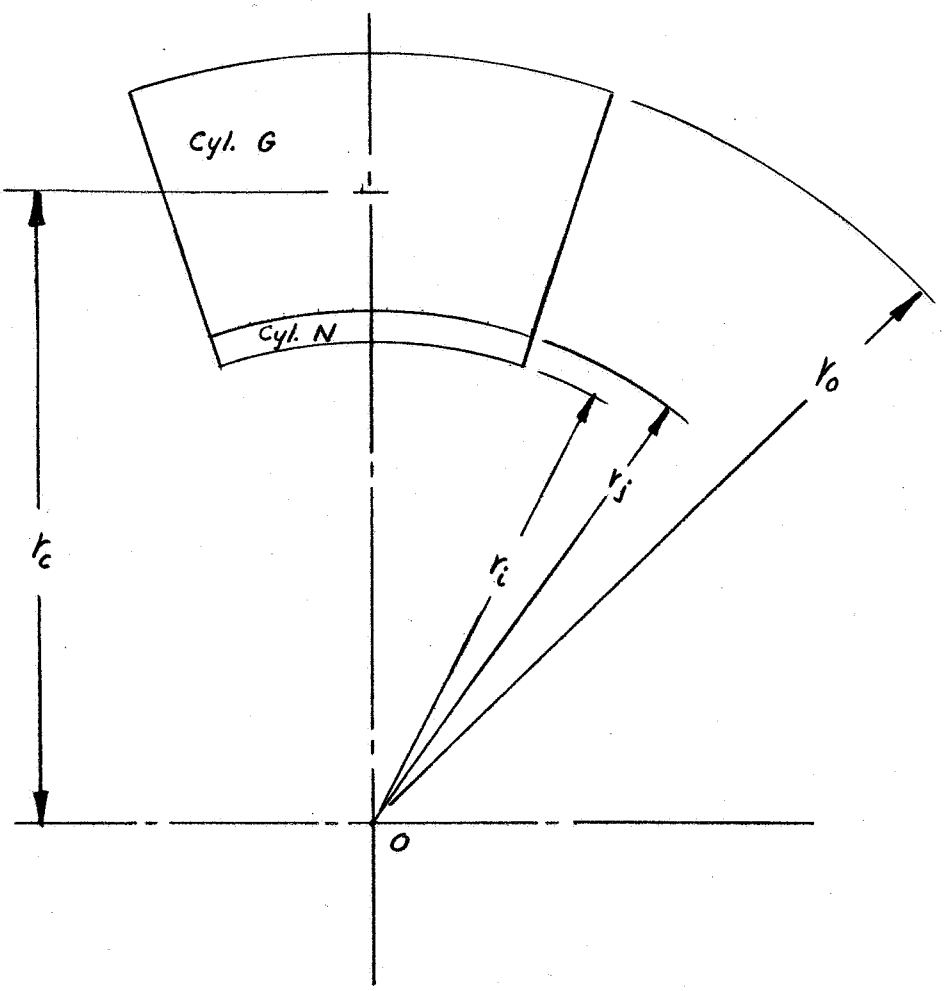

Fig. 20. - Sketch of composite cylinder.

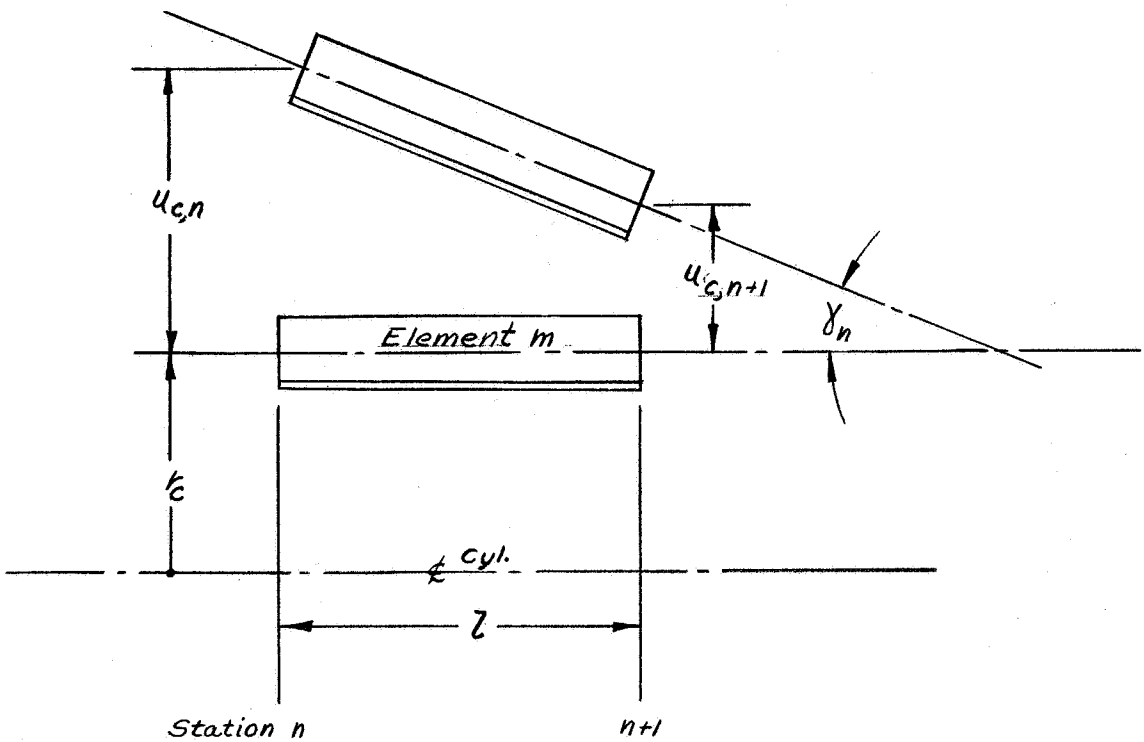

Fig. 21. - Rigid body rotation of element m at stations n and n + 1.

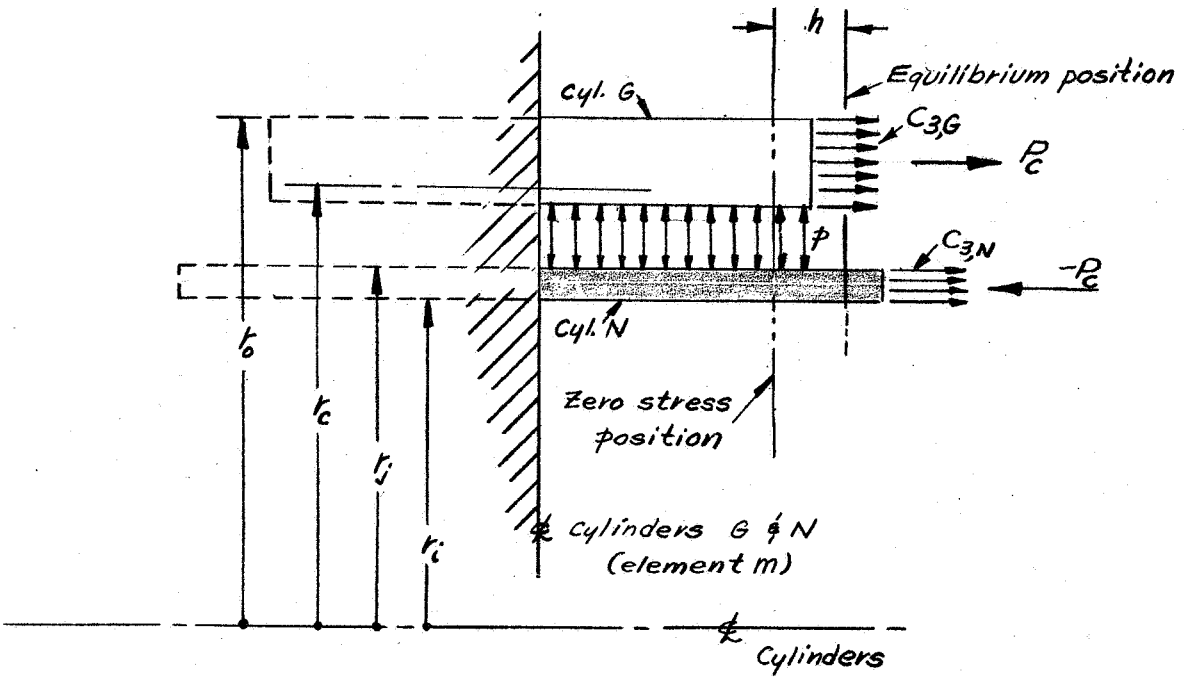

Fig. 22. - Determination of couple force P_c and contact pressure p.

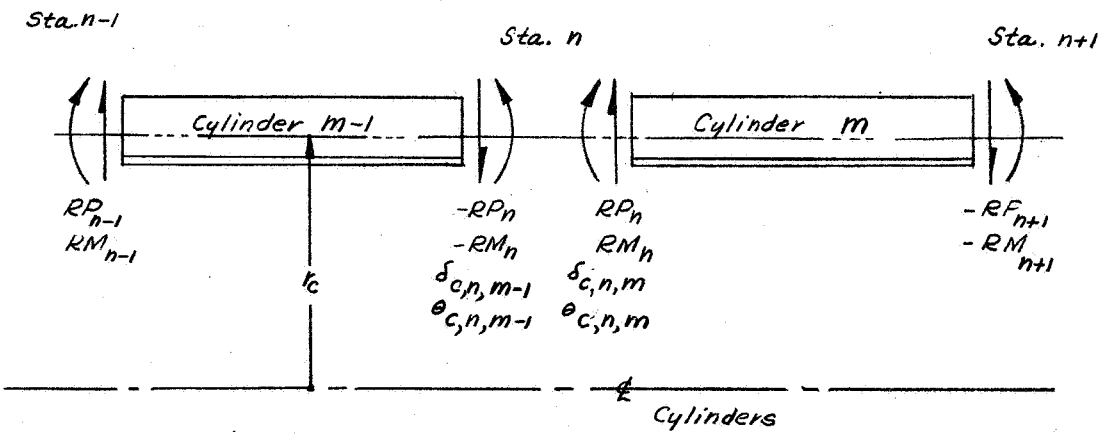

Fig. 23. - Deflection and rotation compatibility between finite cylinders at r_c.

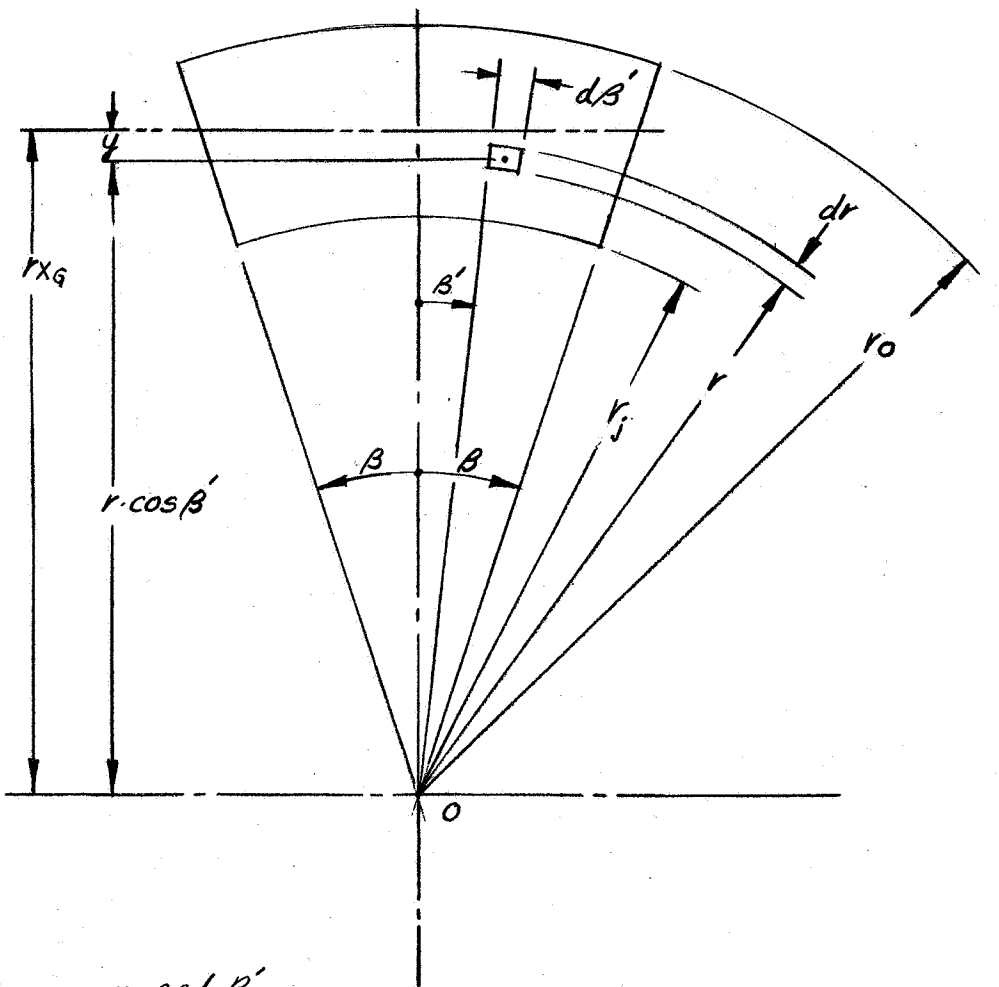

Limits on r and β'

$r_j \leq r \leq r_o$

$-\beta \leq \beta' \leq \beta$

where $2\beta = .01$ radians

Fig. 24. - Moment of inertia - sector of a cylinder.

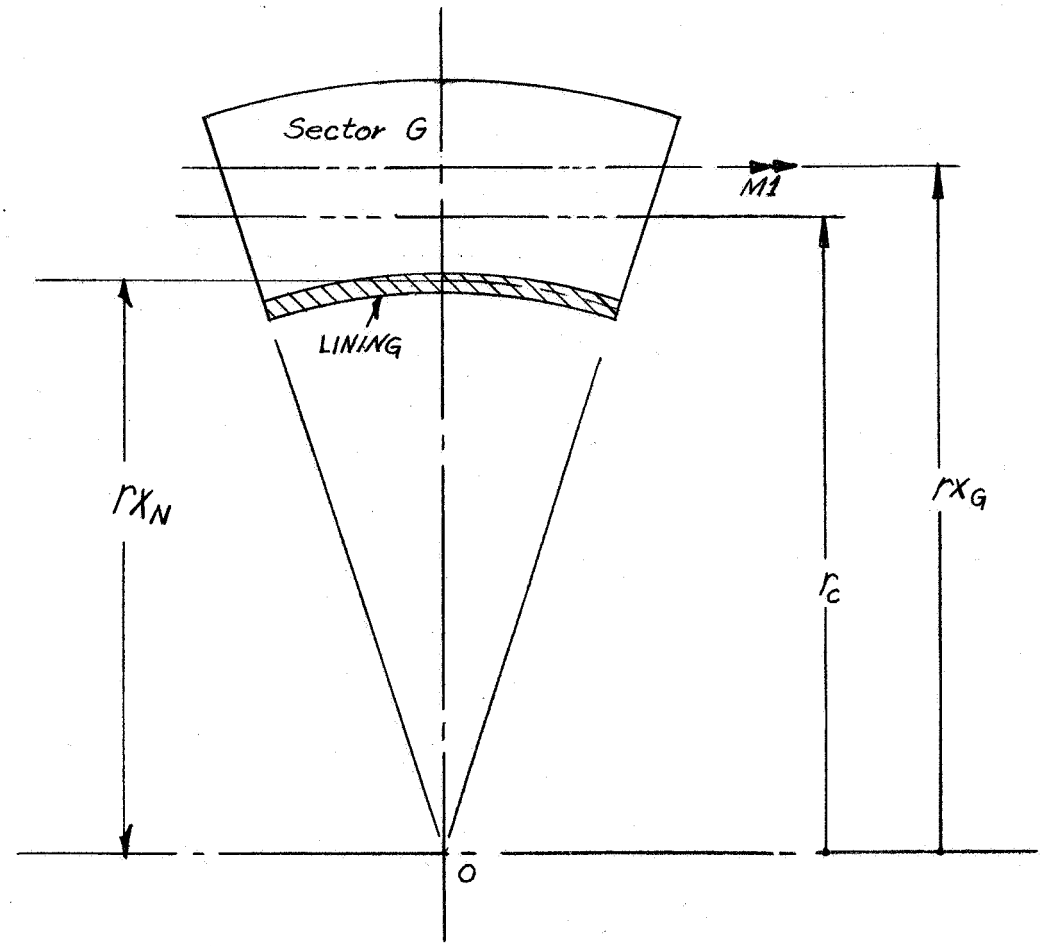

Fig. 25. - Neutral axis of a composite section.

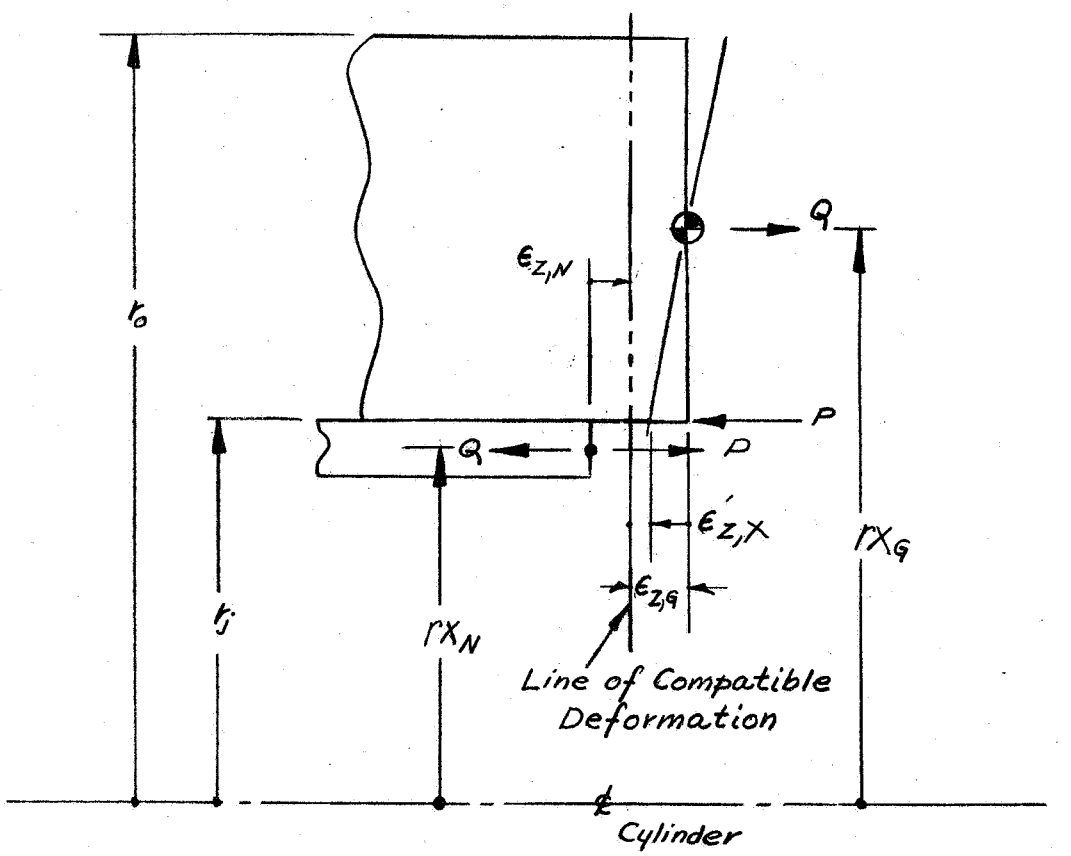

Fig. 26. - Resistance to bending and elongation due to M = 1 in. lb.

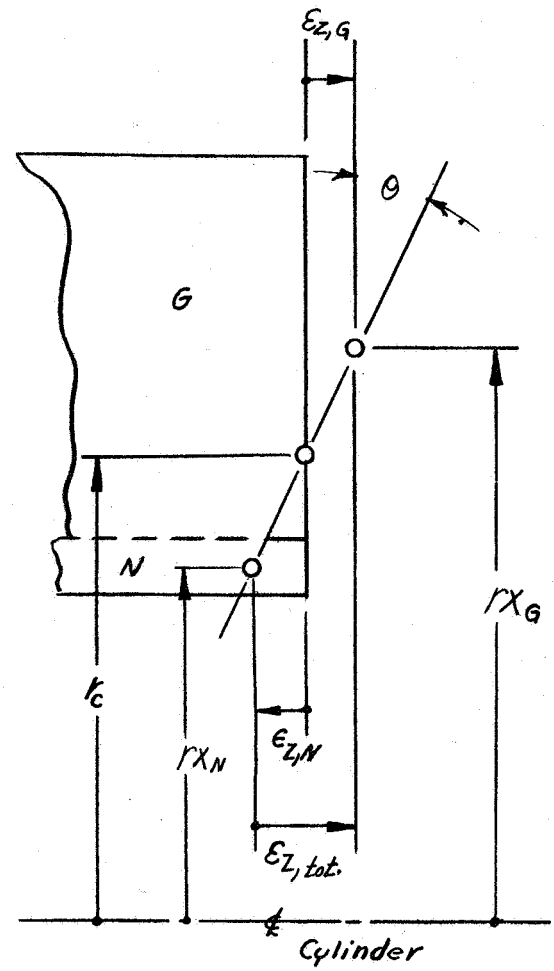

Fig. 27. - Total uniform axial strain $\varepsilon_{z,\,tot.}$

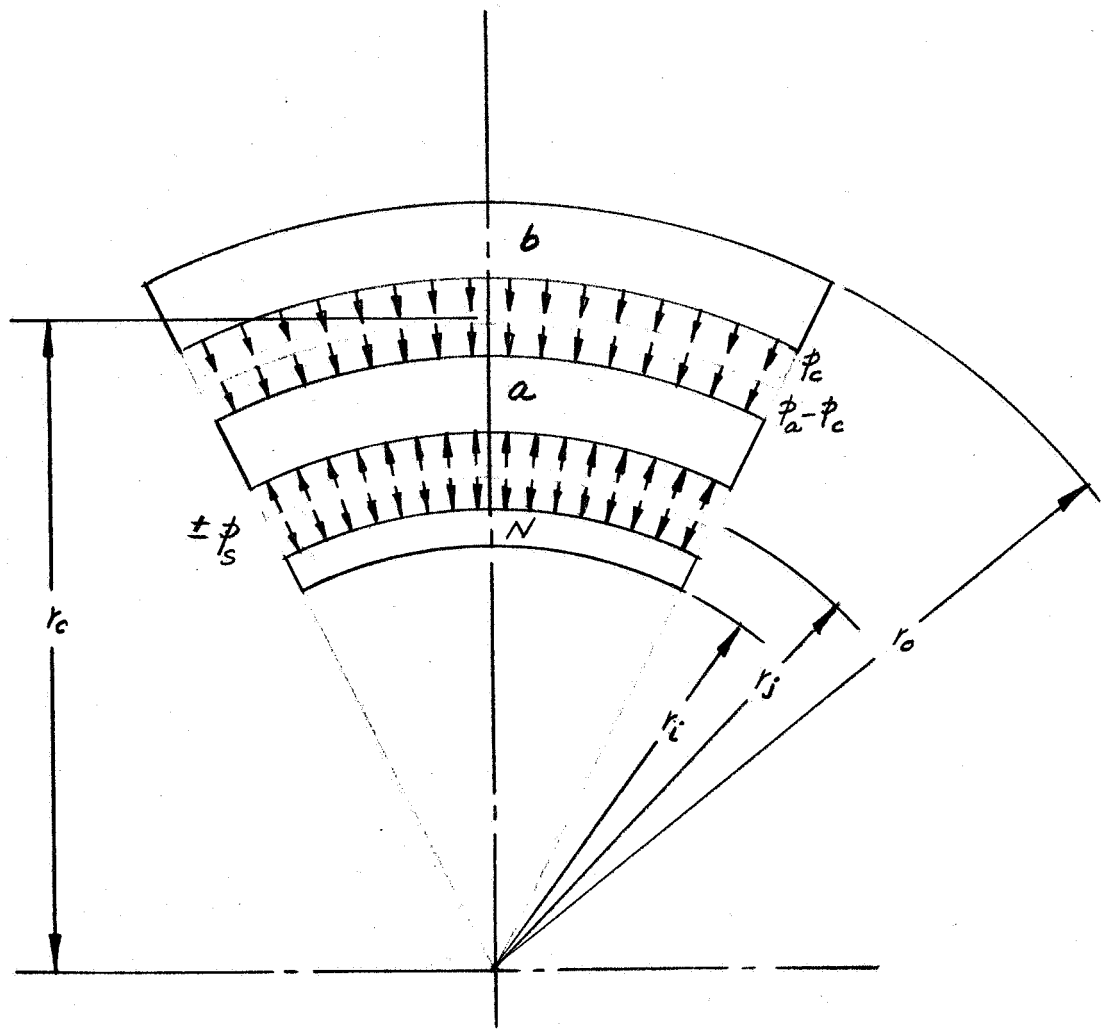

Fig. 28. - Spring constant of a composite sector.